



Quantitatively Monitoring Bubble-Flow at a Seep Site Offshore Oregon: Field Trials and Methodological Advances for Parallel Optical and Hydroacoustical Measurements

Mario E. Veloso-Alarcón^{1*}, Peter Urban^{1,2}, Tim Weiss¹, Kevin Köser¹, Mengkun She¹ and Jens Greinert^{1,3}

¹GEOMAR Helmholtz Centre for Ocean Research Kiel, Kiel, Germany, ²Department of Geology and Department Data Analysis and Mathematical Modeling, Ghent University, Ghent, Belgium, ³Institute of Geosciences, Christian-Albrechts University Kiel, Kiel, Germany

OPEN ACCESS

Edited by:

Andreas Lorke,
University of Koblenz and Landau,
Germany

Reviewed by:

Binbin Wang,
University of Missouri, United States
Ian MacDonald,
Florida State University, United States

*Correspondence:

Mario E. Veloso-Alarcón
mveloso@geomar.de

Specialty section:

This article was submitted to
Marine Geoscience,
a section of the journal
Frontiers in Earth Science

Received: 20 January 2022

Accepted: 10 June 2022

Published: 22 July 2022

Citation:

Veloso-Alarcón ME, Urban P, Weiss T, Köser K, She M and Greinert J (2022) Quantitatively Monitoring Bubble-Flow at a Seep Site Offshore Oregon: Field Trials and Methodological Advances for Parallel Optical and Hydroacoustical Measurements. *Front. Earth Sci.* 10:858992. doi: 10.3389/feart.2022.858992

Two lander-based devices, the Bubble-Box and GasQuant-II, were used to investigate the spatial and temporal variability and total gas flow rates of a seep area offshore Oregon, United States. The Bubble-Box is a stereo camera-equipped lander that records bubbles inside a rising corridor with 80 Hz, allowing for automated image analyses of bubble size distributions and rising speeds. GasQuant is a hydroacoustic lander using a horizontally oriented multibeam swath to record the backscatter intensity of bubble streams passing the swath plain. The experimental set up at the Astoria Canyon site at a water depth of about 500 m aimed at calibrating the hydroacoustic GasQuant data with the visual Bubble-Box data for a spatial and temporal flow rate quantification of the site. For about 90 h in total, both systems were deployed simultaneously and pressure and temperature data were recorded using a CTD as well. Detailed image analyses show a Gaussian-like bubble size distribution of bubbles with a radius of 0.6–6 mm (mean 2.5 mm, std. dev. 0.25 mm); this is very similar to other measurements reported in the literature. Rising speeds ranged from 15 to 37 cm/s between 1- and 5-mm bubble sizes and are thus, in parts, slightly faster than reported elsewhere. Bubble sizes and calculated flow rates are rather constant over time at the two monitored bubble streams. Flow rates of these individual bubble streams are in the range of 544–1,278 mm³/s. One Bubble-Box data set was used to calibrate the acoustic backscatter response of the GasQuant data, enabling us to calculate a flow rate of the ensonified seep area (~1,700 m²) that ranged from 4.98 to 8.33 L/min (5.38 × 10⁶ to 9.01 × 10⁶ CH₄ mol/year). Such flow rates are common for seep areas of similar size, and as such, this location is classified as a normally active seep area. For deriving these acoustically based flow rates, the detailed data pre-processing considered echogram gridding methods of the swath data and bubble responses at the respective water depth. The described method uses the inverse gas flow quantification approach and gives an in-depth example of the benefits of using acoustic and optical methods in tandem.

Keywords: methane seeps, bubbles, hydroacoustic quantification, GasQuant-II, optical bubble measurements, Bubble-Box, Astoria Canyon

1 INTRODUCTION

1.1 Methane Seepage

For almost 40 years, scientists have studied the global phenomena of natural methane release from underwater seepage areas at different geological settings (see overview in Suess, 2014). This research has covered different aspects of methane seepage, including their ability to sustain chemoautotrophic ecosystems and microbial communities (Boetius et al., 2000; Sahling et al., 2002; Levin et al., 2016), their geological past and their manifestation in methane derived carbonates (Greinert et al., 2001; Campbell, 2006; Liebetrau et al., 2010), their link to gas hydrates and hydrocarbon reservoirs (Westbrook et al., 2008; Smith et al., 2014; Ruppel and Kessler, 2017), or the potential transport of methane into the atmosphere and its relevance to global atmospheric methane concentrations (Etiope, 2009; Shakhova et al., 2010; Kirschke et al., 2013; Pohlman et al., 2017; Römer et al., 2017; Weber et al., 2019). To answer these questions, scientists have tried to elucidate in detail the mechanism of bubble seepage and its triggers including internal forcing (source depletion and refilling and clogging of pathways) or external forcing (pressure changes, e.g., due to tides, tectonic activity, or sea-level changes) (Westbrook et al., 2009; Berndt et al., 2014; Shakhova et al., 2014; Wallmann et al., 2018).

In all these studies, the key aspects for properly interpreting the spatio-temporal modulations of a bubble seepage area are their quantitative assessment and their accurate geo-reference. For more than a decade, the quantification and positioning of seepage occurrences have been performed using independent or combinations of optical and remote hydroacoustic methods as well as direct sampling techniques (Sauter et al., 2006; Nikolovska et al., 2008; Sahling et al., 2009; Weber et al., 2014). In most cases, only local measurements could be undertaken when, for example, ROVs performed the direct measurement. Others allowed for longer, lander-based, studies at a single release location, seep area (e.g., Leifer and Boles, 2005; Greinert, 2008; Schneider von Deimling et al., 2011; Kannberg et al., 2013), or entire margins (Skarke et al., 2014; Leifer et al., 2017; Riedel et al., 2018); yet another set of studies revisited the same area several times to investigate seep activity and location changes over days (Jerram et al., 2015) to years (Römer et al., 2017; Urban et al., 2017; Veloso-Alarcón et al., 2019). Only few studies allowed for a quasi-continuous evaluation of temporal variability, for example, at the monitoring site Barkley Canyon of the Ocean Networks Canada cable observatory for seep-related biological activity or gas hydrate and seepage dynamics (Römer et al., 2016; Doya et al., 2017; De Leo et al., 2018).

1.2 Investigation Methodologies

Optical observatories employing simple (only a camera and scale) or more sophisticated devices (back-illuminated bubble chambers with high-speed cameras) are commonly deployed and

positioned by ROV or divers (Leifer et al., 2000; Rehder et al., 2002; Rehder et al., 2009; Leifer and Culling 2010). These techniques are rather straightforward in theory and very precise in determining bubble sizes and rising speeds, once the hurdle of fast enough acquisition of high-resolution images and subsequent processing of high amounts of data is overcome. Recent improvements include stereoscopic imaging techniques for characterizing bubble release that have been successfully tested under controlled conditions (Wang and Socolofsky, 2015; She et al., 2022) as well as *in situ* (Wang et al., 2016; Razaz et al., 2020; Wang et al., 2020). These are, however, limited (by the range of visual observation) to a distance of a few meters, making active acoustic approaches in combination with optical observatories the method of choice for the quantification of bubble emissions of large areas. Alternatively, passive acoustics has emerged as a new supporting technique for quantitative monitoring of seep areas, including CO₂ CCS areas (Bergès et al., 2015; Li et al., 2020a; Longo et al., 2021; Caudron et al., 2022). Moreover, the combination of hydroacoustics and optical techniques has also been used for studying the dissolution of bubbles within the water column, including the validation of models for mass transfer and bubble transport for natural bubble seepage (Wang et al., 2020).

In contrast to optics, active and passive hydroacoustic systems do not provide direct measurements of the bubble amount and sizes, and quantification is achieved by the sonar signal inversion. Subsequently, a robust method for quantitative assessment of bubble flow rates relies on a very good understanding of the used hydroacoustic technology and the theoretical background of the acoustical backscattering response of bubbles. Particularly, over the last decade, active hydroacoustic systems have been employed during research cruises for mapping bubbling seep areas and quantitative assessments using single beam echosounder systems (SBES; Kannberg et al., 2013; Weber et al., 2014; Veloso et al., 2015; Turco et al., 2022) or multibeam echosounder systems (MBES; Römer et al., 2017; Higgs et al., 2019). Most published quantification methods used hydroacoustic inversion techniques of calibrated SBES parameters as target strength and volume backscattering strength, including the input of optically or acoustically derived bubble size distributions; fewer attempts have been made only using MBES data (e.g., Scandella et al., 2016). The inversion of the MBES signal is still challenging since most of the commercially available echosounder systems, with a few exceptions (e.g., Kongsberg ME70 and iXblue SeapiX), are un-calibrated systems. Compared to the calibration effort for SBESs, calibrating MBESs is more complicated and not yet a standard procedure. Additionally, a very good knowledge about the internal processing steps from signal detection to data recording is important for correctly processing MBES data for gas flow quantifications. As the knowledge about the exact processing is often proprietary information, it is sometimes difficult to get.

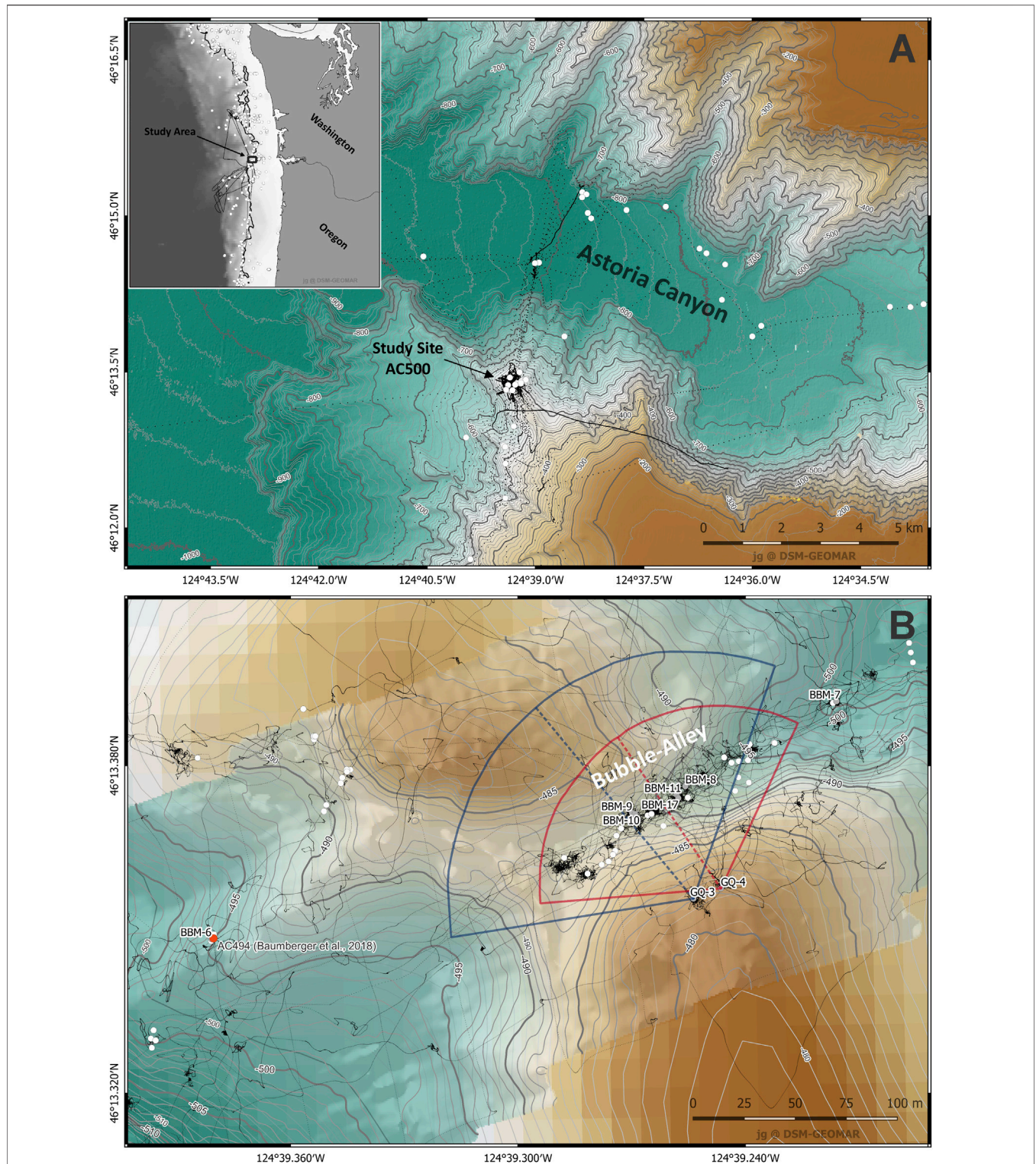


FIGURE 1 | (A) Bathymetric map of the Astoria Canyon area, with the Study Site AC500 on the ridge crest as part of the southern canyon flank. White circles indicate active seep sites detected during MBES surveys from several cruises. Small black spots indicate the cruise track of RV FALKOR. Previously sample seep locations by Baumberger et al. (2018) are given (bathymetric data courtesy of the USGS). **(B)** Detailed map of the AC500 site; bathymetric data have been acquired using the GasQuant Imagenex MBES mounted on the ROV during a mapping survey (Dive 272). All BBM sites are indicated; BBM-11 and BBM-17 locations were close to each other in the middle of the Bubble-Alley. **(A,B)** White dots indicate bubble locations that were annotated during the dives (not all locations are shown), and small black dots are ship **(A)** and ROV tracks **(B)**.

1.3 Data and Scope of the Article

This article describes and analyzes optical and hydroacoustic data from an active seep site offshore Oregon well above the methane hydrate stability zone. The systems used were the lander-based hydroacoustic multibeam system GasQuant-II and the stereo camera-equipped system Bubble-Box (BBox; She et al., 2022), both developed at GEOMAR. The deployments of the systems took place as part of cruise FK190612 with RV FALKOR from the Schmidt-Ocean Institute in June 2019. The cruise was led by the USGS with the aim of investigating gas release above and below the hydrate stability zone at known and new seep sites along the Cascadia continental margin. During the cruise, several sites were investigated during ROV dives and also with GasQuant and BBox deployments, but the data set presented here is only from the Astoria Canyon site AC500 at a water depth of about 500 m (Figure 1). Both systems were simultaneously deployed to measure bubble release activity of individual streams (BBox and GasQuant) and an entire seepage area (GasQuant). The measurements were planned as an *in situ* experiment to 1) monitor and quantify gas bubble release at the site for several days and identify potential internal and external forcing on the release; 2) test and verify an approach for parallel deployment of optical and acoustic systems in which bubble parameters are derived from optical information and then used in the inverse hydroacoustic method for temporally and spatially high-resolution quantifications; and 3) highlight system-dependent and general pitfalls of the acoustic quantification caused by the intricacies during acoustic bubble observations.

In detail, we report on the undertaken processing steps to measure bubble size distributions and flow rates over time from both systems. We highlight the difficulties of acquiring good data and particularly of understanding what the received multibeam signals actually represent. In a final step, we merge bubble size distributions, rising speeds, and backscatter intensity to derive bubble flow rates and the variability from the $\sim 1,700\text{-m}^2$ large seep area. We further discuss bubble flow changes with respect to pressure/tidal, small bubble size variations, and shifts of the bubble location when crossing the acoustic MBES swath. The presented work thus not only presents “another” high-resolution data set about flow rate and temporal variability of gas bubbles at a seep site but also highlights a number of methodological processes that greatly influence the analyses, but are rarely or not considered in many other publications. Furthermore, the presented work provides new insightful information regarding *in situ* MBES calibration using simultaneous optical information, as well as indicating the challenges, the problems, and their possible solutions toward advancing the technique.

1.4 Study Area

The study area lies in a gully-like depression on a ridge crest belonging to the southern slope of the Astoria Canyon system (Figure 1A). As such, the area is part of the accretionary prism of the Cascadia margin formed due to the subduction of the Juan de Fuca plate beneath North America. Due to this accretion and the proximity to land and therefore high organic and terrestrial sediment input, the entire region of Cascadia is characterized by the widespread occurrence of active and past methane seepage

that make this region one of the most renowned methane seep areas in the world. Locations like Hydrate Ridge (Suess et al., 1999; Torres et al., 2002; Kannberg et al., 2013) or Coil Oil Point (Leifer and Culling, 2010; Schmale et al., 2015) further to the south or Barkley Canyon to the north (Römer et al., 2016; Doya et al., 2017) are part of this larger seep region. Figure 1B shows the detailed location of our study and seep site AC500. During cruise FK190612, the wider area of the canyon was studied during several ROV dives and hydroacoustic surveys, showing that a number of already known seep sites were still active whereas new sites, for example, at the edge of the flat canyon infill to the northern canyon slope, were newly discovered. The AC500 sites was known before the cruise through investigations in 2016 during expedition NA072 with E/VNautilus where visual inspections and gas sampling indicated several seep locations with secondarily oxidized biogenic methane being expelled (Baumberger et al., 2018). To repeat gas analyses at site AC494 from the study by Baumberger et al. (2018), the area was revisited with ROV SuBastian during dive 262 and the “Bubble-Alley” within an ENE striking gully-like valley about 150 m east of site AC494 was discovered and inspected more closely (Figure 1B). Over a distance of about 150 m, many bubble release sites occur in the sandy seafloor, and more than 100 isolated bubble streams or clusters of them were encountered during live annotation of bubble occurrences as well as during subsequent re-annotation of the video footage. A total of seven ROV dives, including dive 262, were performed at site AC500 (other SuBastian dives were 263, 264, 266, 272, 273, and 276), during which the Bubble-Alley was sampled repeatedly with the BBox and visually inspected for seep-related features such as bubble release, chemoautotrophic fauna, and methane-derived authigenic carbonates.

2 DATA, EQUIPMENT, AND METHODS

2.1 Data Sets

Of the seven ROV dives at the AC500 site, three were used to deploy GasQuant and the BBox in parallel for several days; a total of seven BBox measurements (BBM) and three GasQuant measurements (GQM) were undertaken. In this study, we only present and discuss data from BBM-11 and GQM-3 (dives 264–266) and BBM-17 and GQM-4 (dives 272–276) as these have the needed spatial and temporal overlap for reaching our measurements goals (details see Table 1). Both systems were placed accurately by the ROV on the ground, and the transducer head of the GasQuant system was oriented toward the direction of the bubble source, using the compass and manipulator of the ROV to rotate and tilt the transducer head accordingly. The general system parts and functions are briefly described below, followed by a more detailed data processing section.

2.2 Bubble-Box System

The Bubble-Box System (BBox, Figure 2A–C) is a compact, ROV-deployable photogrammetric system designed to acquire black and white images for an automatic analysis of bubbles larger than 0.5 mm in diameter. The purpose of the system is to derive

TABLE 1 | Deployment details of the BBox and GasQuant measurements at the AC500 site.

Deployment	ROV dive	Start (2019; UTC)	Stop (2019; UTC)	Depth (m)	Latitude and longitude	System settings
BBM-11	264	19 June, 16:35	21 June, 09:44	490	46.22291153 N 124.65430253 W	1 min recording, 14 min off, 80 images per second
GQM-3	264	19 June, 15:13	21 June, 21:13	482	46.22261273 N 124.65422939 W	120° swath, 80 m range, 480 μ s pulse length, 500 samples for entire range, view direction toward \sim 320°
BBM-17	272	27 June, 16:21	29 June, 19:34	490	46.22290054 N 124.65429503 W	1 min recording, 14 min off, 80 images per second
GQM-4	273	28 June, 13:40	30 June, 06:40	482	46.2226344 N 124.65410701 W	120° swath, 60 m range, 360 μ s pulse length, 500 samples for entire range, view direction toward \sim 325°

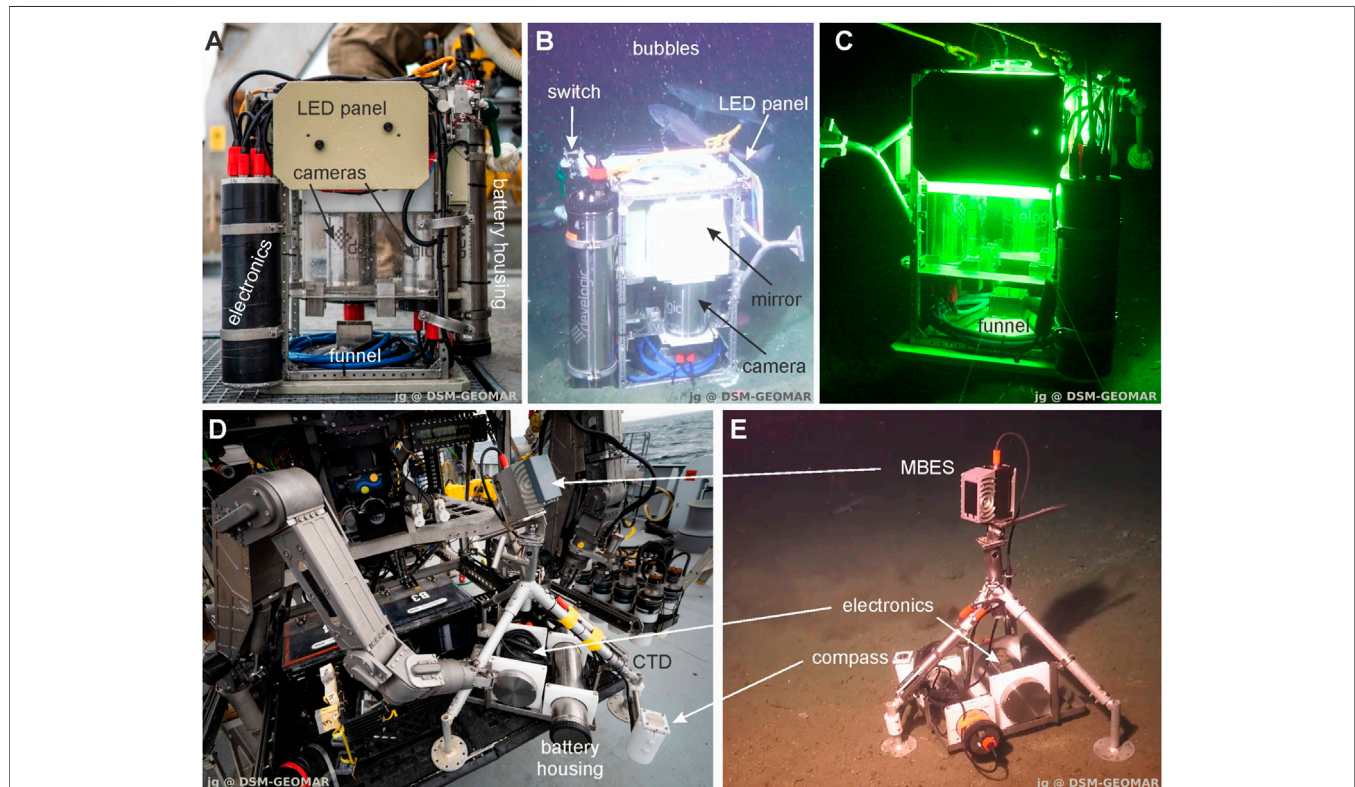


FIGURE 2 | BBox on deck (A), on the seafloor (B), and turned on with flushing LEDs (C). Shown are the different components. In (B,C), bubbles can be seen escaping the BBox on the top; C also shows bubble within the BBox. GasQuant II lander system before deployment on the ROV (D) and located on the seafloor (E) with main parts of the system indicated.

bubble size distributions (BSD), bubble rising speeds (BRS), and the shape and number of the bubbles per time (Figure 2; She et al., 2022). This can be used to directly quantify free gas flow rates and get important input parameters such as size and rising speed for hydroacoustic gas flow quantifications. Two synchronized and photogrammetrically calibrated machine vision cameras take images with a back-illuminated setting (bright-field), where each bubble is photographed from two perspectives of 90° difference. With each image pair, individual bubble positions and shapes can be measured precisely (1% diameter uncertainty) and bubble rising speeds can be determined over time. The upward installed cameras in their

6,000-m pressure-resistant housings look through a 45° tilted mirror at a bubble rise corridor to keep a compact size of the instrument. The lenses are carefully centered within the dome ports to minimize refraction at the air–glass–water interfaces (She et al., 2019). To maximize bubble contrast, a set of four green LEDs (550 nm) is mounted behind acrylic diffuser plates opposite to each camera. The LEDs flash at 80 or 100 Hz to save energy, and a microcontroller triggers the camera at each flash to acquire two synchronized images exposed for 1 ms. Power for the complete system is provided by a container for exchangeable batteries (Figure 2B). An additional pressure housing contains the electronics for distributing the power and synchronizing

signals. It further contains the driver circuits for the LEDs. The BBox has a mechanic switch which allows for turning the system on and off by the ROV when in the water.

ROV SuBastian deployed the BBox by placing it as straightly as possible onto the selected bubble release source (e.g., youtube-video-FK-Dive264, video time: ~min 37). The open structure on one side of the box allows for monitoring the rising bubbles through the box and their escape through an opening at the top. A funnel at the bottom of the box ensures that bubbles enter the 8 cm by 8 cm wide rise corridor in the center of the box, where they are recorded by the two cameras. Once the BBox was in position, the measurement was started, using the switch to turn power on. A much more detailed description of the BBox, its technical specifications, and processing steps are given in the study by She et al. (2022).

Prior to deployment, the computer times were synchronized to UTC time and the setting parameters were set (Table 1). Upon recovery of the system, data were downloaded and visually inspected to check data quality. In general, bubbles were successfully captured by the two cameras with the exception of some time-intervals when the camera dome ports were blocked by sediment and/or animals (sea urchins) or when the observed bubble stream moved out of the camera field of view. The latter happened in two deployments when the BBox sank into the sediment and lost its upright orientation. Example images are provided as **Supplementary Figure S4**. Prior to and after the cruise, the two cameras were photogrammetrically calibrated in the laboratory (She et al., 2022), but re-calibration was necessary for the *in situ* acquired images because slight movements of the mirrors and camera housings occurred due to the increased pressure and lower temperature at depth. Thus, slight adjustments of the *in situ* calibration were derived by manually selecting a subset of images from the entire observation time; it was verified that the same re-calibration parameters can be used for all deployments. The BBox data were processed as discussed in the study by She et al. (2022) and results include individual bubble sizes (mm radius of the volume equivalent sphere) and rising speeds (cm/s), the number of bubbles per time (n/s), and the respective volume flow rates (ml/s). Three data sets could be derived, one for each camera individually (camera 1 and 2) as well as the stereo matching result. The automated recording was set to one minute of recording every 15 min which results in about 3,600–4,000 images per interval used for bubble analyses. The data of the two BBox deployments are published on PANGAEA (Veloso-Alarcón et al., all BBox related post-processed data will be submitted soon; the DOI will be added in the final article).

2.3 GasQuant II System

The GasQuant II system is a hydroacoustic lander with a horizontally oriented multibeam swath for performing long-term observations of bubble release activity of an entire seep area. In contrast to a vertically oriented swath, which needs to be mechanically rotated (e.g., Römer et al., 2017), a vertically oriented swath enables us to monitor the target area continuously without spatial or temporal gaps for the entire 120°-wide swath. GasQuant II (Figures 2D,E) was built as the successor of the original, much larger GasQuant system (Greinert, 2008), which has been successfully used for tempo-spatial variability measurements of gas releases in the Black Sea and North Sea (Greinert, 2008; Schneider von Deimling et al., 2011). GasQuant

II uses an Imagenex 837B Delta T multibeam as its primary sensor (similar to the work of Scandella et al., 2016 and Römer et al., 2017). The transducer has a maximum opening angle of 120°, comprises 120 beams, and transmits at 260 kHz. The beam opening angles as given by the manufacturer are 3° by 3°; no details are given about the suppression level of the side lobes. The measurement range extends from 5 to 100 m and can be set at nine different discrete levels of the maximum recording range. The Imagenex provides 500 data values (independent of the range) for each beam that represents voltage levels proportional to the backscattered acoustic pressure, the applied time-varying gain, and a constant gain (the start and display gains of the system). The time-varying gain compensates the propagation loss for volume backscattering (named extended target by the manufacturer). These values can be converted to un-calibrated amplitudes proportional to backscatter volume strength values as described in **Supplementary Section 1**. It needs to be noted that these un-calibrated amplitudes are possibly angle dependent (where in the swath, the backscatter target exists) as shown by Scandella et al. (2016). Thus, an angular correction of the backscatter amplitudes of the echogram might be required. The multibeam is installed on top of a tripod at a height of 1.25 m (Figures 2D,E). A Sea and Sun CTD is attached to the tripod to record pressure, temperature, and conductivity, used for investigating pressure changes over time and to derive the ambient sound velocity in real time and feed it into the Imagenex for sound velocity adaptations. A magnetic compass provides information about the orientation of the lander general view direction of the transducer. Electric power of 3 kWh is provided by lithium battery cells installed in a housing for exchangeable batteries. The power is distributed to the different sensors through the additional electronics housing that holds the control computer and logging unit for the multibeam and CTD. The system is preprogrammed to start at a certain time, and it is stopped manually upon recovery. The system was deployed with the ROV and placed on the seafloor using its manipulator (e.g., youtube-video-FK-Dive264, video time ~min 16). In total, five deployments were conducted during FK190612, but only GQM-3 and GQM-4 are used in this study. **Table 1** summarizes settings, date-time information, and position of the GasQuant deployments. The data of the two GasQuant deployments presented here are published on PANGAEA (Veloso-Alarcón et al., all BBox related post-processed data will be submitted soon; the DOI will be added in the final article). A detailed description about data quality is given in **Supplementary Section 2**. Because the processing of the acoustic data is essential for correct interpretation of the data, the different processing steps are explained in more detail here.

2.4 GasQuant Data Processing

2.4.1 MBES Data Correction

The first step in processing was correcting the Imagenex MBES data for transmission loss due to sound absorption. The original absorption of 0.1 dB/km was replaced by new values calculated using the recorded CTD data and applying the empirical relation of Francois and Garrison (1982). Absorption values and ambient parameters used for the deployments GQM-3 and GQM-4 are presented in **Supplementary Table S1**. Un-calibrated volume backscattering values (A_V) along each beam were calculated using the recorded amplitude/voltage values A_{rec} of the system

(**Supplementary Equation S.1**). Due to lack of our own experimental calibration, the angular correction of A_V was not applied.

2.4.2 MBES Data Gridding and Interpolation

For quantitative analysis of MBES water column imaging data (WCI), it must be acknowledged that volumes of neighboring acoustic samples from adjacent beams physically overlap. Summing up measurements of neighboring beams to a combined value would therefore lead to an overestimation of the measured gas flow depending on the exact beam overlap. To overcome this problem, we applied the gridding method presented by Urban et al. (2022), in which un-calibrated volume backscattering values A_V (proportional to volume backscattering) of the ping-based WCI data were gridded onto a two-dimensional voxel grid by calculating an average acoustic value from all samples in the vicinity of each voxel (voxel weighted mean method from the study by Urban et al., 2022). Voxel volumes were set to 0.7 m by 0.7 m horizontal and 1 m vertical (Δx , Δy , and Δz). A horizontal size of 0.7 m was determined as a lower limit before the voxel-grid started to have empty voxels because of the sample spacing between beams at a larger range. Temporarily, pings were averaged over 60 s although the ping rate was set to 6.3 and 7.6 pings per second for GQM-3 and -4, respectively. The gridded un-calibrated volume backscattering values $A_V(i,j)$ are multiplied by their voxel volume to obtain un-calibrated acoustical cross-section values $A_{bs(i,j)}$ that are proportional to the total backscattering cross-section within each voxel (**Eq. 1**):

$$A_{bs(i,j)} = A_V(i,j)\Delta x\Delta y\Delta z \quad (1)$$

Due to the limited acoustic resolution (wide beam opening angle of 3°), gridded amplitudes may include backscatter signals from other targets in the water column which are physically not located in the respective grid voxels. Urban et al. (2022) showed that the summation of the gridded voxels $A_{bs(i,j)}$ (**Figure 3**) approximates to a value proportional to the total backscattering cross-section of the targets within the ensonified volumetric section of the total backscattering cross-section σ_{bsT} . In this case, σ_{bsT} can be written as follows:

$$\sigma_{bsT} = kA_{bsT} \quad (2)$$

where k is a constant representing the proportionality between the real and the un-calibrated total backscattering cross-section. The value k was approximated through theoretical considerations as indicated in **Supplementary Section 1 (Supplementary Eq. S.6)**.

2.4.3 Seep-Anomalies Tracking and Amplitude Determination

The interactive display of consecutive echogram voxel grids allowed for visual identification of acoustic anomalies potentially related to gas seepage in the monitored area (e.g., **Supplementary Figure S5; Supplementary Videos 1 and 2**). Since bubbles move laterally with currents, their acoustic signals change position within the echogram. Two algorithms were

applied for tracking these locations over time (**Supplementary Section 3**). None of the algorithms always worked successfully, especially in areas where acoustic artifacts, noise, and reverberation occasionally masked the bubble seepage signal. In such cases, an interactive method implemented in MATLAB was used which allows for a 3D visualization of the data around the potential seep location with time as the z-axis (**Supplementary Figure S5**). Signals outside of a continuous signal trend can be interactively deleted before the cell with the maximum backscatter value for each ping is detected and determines the central position of the seep spot. This interactive approach was performed when the automated tracking failed (about 30% of the seep spot locations needed manual interaction).

A representative (un-calibrated) backscatter amplitude of the respective seep-anomaly A_{bsT} was calculated by the exponential summation of all $A_{bs(i,j)}$ values within a 5 by 5 voxel area around the tracked central seep-anomaly voxel (i.e., $10 \log \sum_{5 \times 5 Area} 10^{A_{bs(i,j)}/10}$). Alternatively, the overall amplitude of the entire echogram fan (OVA) was calculated by integrating the gridded-voxels (i.e., $10 \log \sum_{FAN} 10^{A_{bs(i,j)}/10}$). This was done for performing activity analysis assuming that the total amplitude modulation was only affected by mobile targets (e.g., bubbles) and backscatter from static reflectors such as the seafloor remained constant. Additionally, the fan was spatially masked where the seafloor was clearly identified. Subsequently, the overall amplitude of the echogram fan excluding the masked region (OVA-masked) was calculated in the same way as explained for the OVA time-series. Both OVA and OVA-masked time series were obtained for GQM-3 and GQM-4 deployments.

2.5 Acoustic Bubble-Flow Rate Quantification

2.5.1 Calibrating GasQuant Acoustic Data With BBox Measurements

The approach of our trials is to use verified bubble-flow rates from the BBox to derive a scaling factor for correlating the acoustic seep-anomaly signals seen in the GasQuant MBES echogram data. Thus, at least one BBox-observed bubble stream needs to be matched with one of the acoustic anomalies within the echogram of the corresponding GQM. To find the BBox location in the MBES-echogram, first, the navigational data of the GasQuant and BBox locations were used and the echograms corresponding to the time when the BBox was placed on the seep-spot were investigated (youtube-video-FK-Dive264, video time ~16 min). As GasQuant was deployed before, the BBox placement reflections of the ROV itself pinpointed the approximated BBox position in the MBES-echogram.

The selection criteria for the BBox bubble stream include that it should be rather isolated (no other bubble stream in the direct proximity) and that it should consist of one vent that could be completely covered with the BBox funnel. As such, the selected bubble stream was not very strong, and finding an isolated bubble stream was difficult in the Bubble-Alley. Two acoustic anomalies (control acoustic anomalies) were identified and used separately to derive the scaling factor value. Only one set of deployments

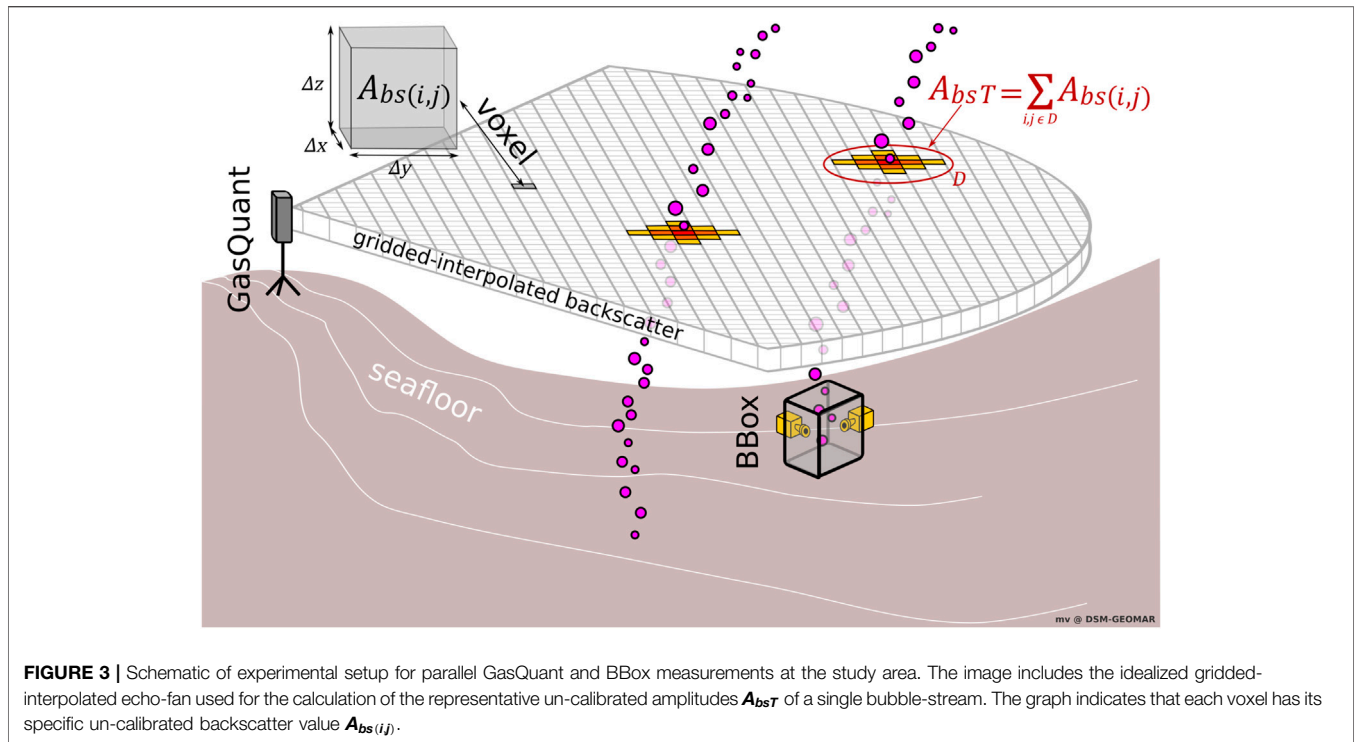


FIGURE 3 | Schematic of experimental setup for parallel GasQuant and BBox measurements at the study area. The image includes the idealized gridded-interpolated echo-fan used for the calculation of the representative un-calibrated amplitudes A_{bsT} of a single bubble-stream. The graph indicates that each voxel has its specific un-calibrated backscatter value $A_{bs(ij)}$.

(GQM-3 and BBM-11) reached the selection criteria and was used for deriving the MBES scaling factor for all GasQuant-based flow-rate quantifications.

2.5.2 Scaling Factor

Within a horizontal-oriented MBES ensonifying a bubble stream with separation between bubbles comparable to the wavelength, the summation of the acoustic backscatter cross-section of gridded voxels σ_{bsT} (Eq. 2) can be approximated by the summation of the theoretical backscatter of the single bubbles (incoherent backscattering; e.g., see Sarkar and Prosperetti, 1993) located within the ensonified parcel of water (Eq. 3).

$$\sigma_{bsT} = \Delta z \sum_{r_i}^{r_f} \frac{N_r}{\Delta t U_r} \sigma_{bs}(r) \tag{3}$$

where

- $\sigma_{bs}(r)$: Theoretical backscattering cross-section of a single bubble in the function of bubble radius r [m²]
- N_r : Number of bubbles of radius r measured in a Δt interval of time [n.° bubbles]
- U_r : Average bubble rising speed of bubbles of radius r [m/s]
- Δt : Time interval of measurement [s]
- r_i, r_f : Initial and final radius size of the bubble size distribution [m]
- Δz : Voxel depth [m]

Equation 3 allows us to calculate the total acoustical cross-section per unit of vertical distance (in this case the voxel depth), based on bubble numbers (N_r) per unit of time (Δ_t) and binned according to

their size, their associated bubble rising speeds (U_r) and the theoretical response of single bubbles. If N_r/Δ_t and U_r are obtained from the ground-truthed BBox measurement and the associated total amplitude A_{bsTG} from the gridded echogram data is known the value of proportionality k from Eq. 2 can be obtained by replacing σ_{bsT} in Eq. 3 with Eq. 2:

$$k = \frac{\Delta z \sum_{r_i}^{r_f} \frac{N_r}{\Delta t U_r} \sigma_{bs}(r)}{A_{bsTG}} \tag{4}$$

where

$$A_{bsTG} = \sum_{i,j \in D_G} A_{bs}(i,j) \tag{5}$$

D_G is the spatial domain (grid cells) containing the voxels of the control acoustic anomaly. If a probability density function of f_r not changing in time is assumed, Eq. 4 can be expressed as follows:

$$k = k_0 \Delta z \sum_{r_i}^{r_f} \frac{f_r}{U_r} \sigma_{bs}(r) \tag{6}$$

Where

$$k_0 = \frac{N_0}{\Delta t A_{bsTG}} \tag{7}$$

$$f_r = \frac{N_r}{N_{TOT}} \tag{8}$$

and

$$\sum_{r_i}^{r_f} f_r = 1 \tag{9}$$

N_r : Total number of bubbles of radius r in the entire data series (binned data).

N_{TOT} : Total number of bubbles counted in the entire data series.

N_0 : Number of bubbles counted at each 1-min data-package analysis.

The value k_0 is defined as the scaling factor which is a constant value used to calibrate the MBES echosounder under the assumption that f_r does not change in time.

2.5.3 Frequency-Dependent Hydroacoustic Bubble Response

We derived the acoustic response of the ensonified section of the bubble stream under the specific ambient pressure conditions by using the theoretical model of Thuraisingham, (1997) with improvements for the damping (Ainslie and Leighton, 2009; Ainslie and Leighton, 2011) as considered by Li et al. (2020b). Values for the ambient conditions and other constants used to perform the model calculations are listed in **Supplementary Table S2**. The resulting acoustical response of single spherical bubbles ranging from 0.05 to 20 mm in radius and ensonified by a monochromatic acoustic signal of 260 kHz is shown in **Supplementary Figure S6**. From this response, it can be seen that the backscatter cross-section TS significantly varies repeatedly for small-size changes. This highlights that bubble size changes of only 0.5 mm could theoretically increase/decrease the backscatter response by up to 40 dB.

2.5.4 Flow Rate Quantification Using the Inverse Method

For deriving the inverse mathematical expression, the flow rate calculation is defined as in **Eq. 10**:

$$\Phi = \frac{N_0}{\Delta t} \sum_{r_i}^{r_f} f_r V_r \tag{10}$$

This expression is multiplied by the ratio (~ 1) between the measured backscatter (**Eq. 2**) and the theoretically predicted backscatter (**Eq. 3**). Considering that the probability density function f_r is non-variant in time and each bubble size has an associated bubble volume V_r and rising velocity U_r), **Eq. 10** can be written as follows:

$$\Phi = k A_{bsT} \frac{\frac{1}{\Delta t} \sum_{r_i}^{r_f} f_r V_r}{\frac{\Delta z}{\Delta t} \sum_{r_i}^{r_f} \frac{f_r}{U_r} \sigma_{bs}(r)} \tag{11}$$

Replacing k with **Eq. 6** in **Eq. 11** results in the simplified flow rate of **Eq 12**:

$$\Phi = k_0 A_{bsT} \sum_{r_i}^{r_f} f_r V_r \tag{12}$$

Note that **Eq. 12** is independent of the backscattering acoustic response when f_r , U_r , and V_r are considered constant through time.

3 RESULTS

3.1 Bubble Sizes and Rising Speeds in BBox Data

The two BBox deployments, BBM-11 and BBM-17, are analyzed in this study. As previously mentioned, the data were occasionally affected by view obstructions (BBM-17) through sediment or sea urchins or the incomplete coverage of the bubble stream (BBM-11) in both cameras, preventing a stereo evaluation. Bubbles could still be counted “manually” assuming the bubble position and 3D shape (monocular approximation). However, we experienced some discrepancies in monocular evaluation when compared to the stereo evaluation, and due to the lower confidence of these intervals, they were excluded from later analysis. In summary, the presented bubble-size-related time series only contain those times where bubble numbers varied by less than 100 between camera 1 and camera 2 and where a stereo matching could be achieved. The final results for the two BBox data sets are shown in **Figure 4** and **Supplementary Table S3**.

In general, the results show no significant variability in bubble sizes within one and between the two measurements. Similarly, the amount of bubbles per time does not vary significantly within each measurement, but they are about twice as high in BBM-17, with ~ 19 bubbles/s compared to only ~ 9 bubbles/s in BBM-11. Thus, the calculated flow rate of BBM-17 is approximately double the one from BBM-11 ($6.55 \text{ cm}^3/\text{s}$ compared to $12.28 \text{ cm}^3/\text{s}$). This indicates that the initial bubble size at release is not changing between different seep spots, but the number of bubbles changes and therefore modulates the flow rate.

For bubble number analyses of any individual 1-min data sets, we considered results from the individual camera observations and excluded the ones from the stereo matching. This is because the number of bubbles analyzed through the stereo matching is lower due to the difficulties in the actual matching. Single bubbles can be measured better using the stereo matching method, but when many bubbles form a bubble stream, some bubbles are occluded by others and leave the observation corridor unnoticed. Conversely, bubble size and rising speed analyses were performed using results from the stereo matching approach since they provide higher confidence. For deriving an average bubble size distribution (BSD), bubbles were binned according to their size in 0.25-mm intervals between 0.5 and 15 mm for both BBM data sets. **Figure 5A** shows the average normalized BSDs from the stereo matching and their combination of both BBM data sets. Similarly, bubble rising speeds (BRSs) from the stereo matching results were binned according to their size. **Figure 5B** shows BRSs for the two deployments together with their combination.

The BSDs of both deployments are roughly Gaussian distributed with a center at about 2.6 mm in radius for similar bubble sizes (BSD BBM-11: ~ 2.6 mm and BSD BBM-17: ~ 2.4 mm). Most of the bubble sizes range from 1 to 4 mm in radii and BRSs vary from 10 to 47 cm/s and are slightly faster for BBM-17 than for BBM-11 (**Figure 5B**). BRS distributions for the two deployments have a local maximum radius around ~ 1 mm, after which the rising speed decreases slightly with increasing bubble size until a bubble radius of 3.5 mm. BRSs of bubbles

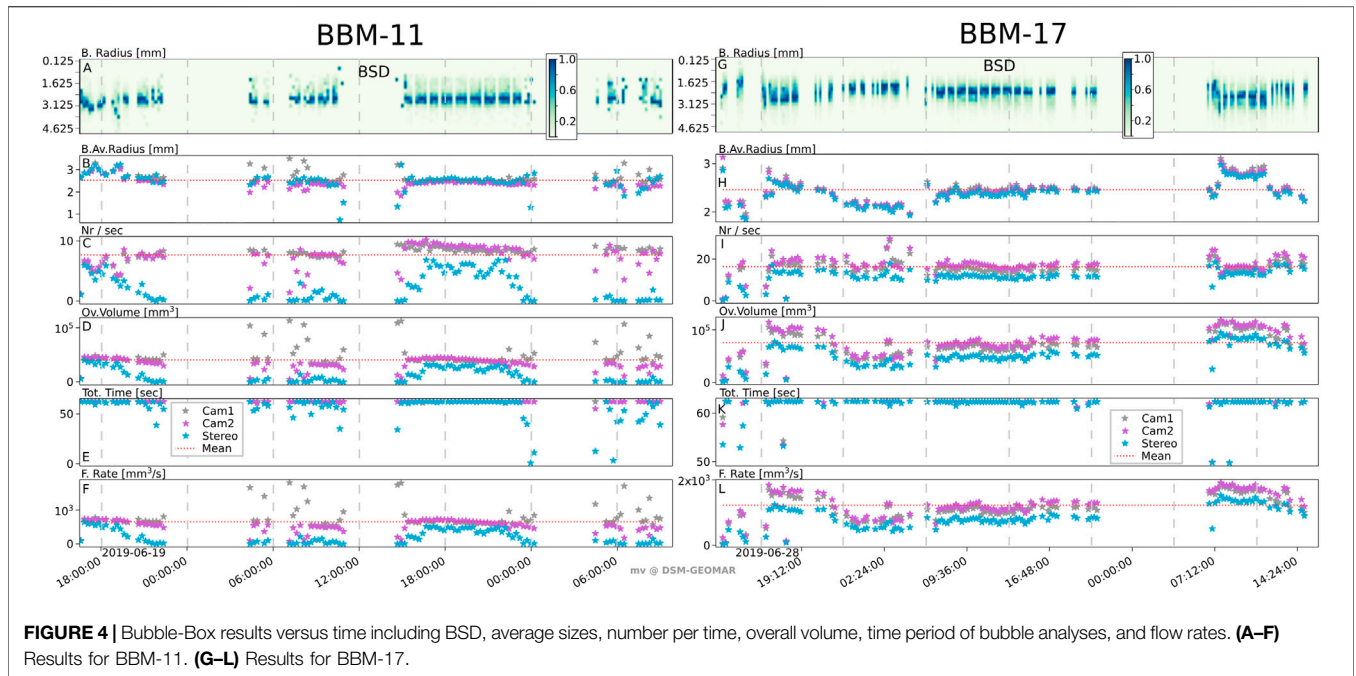


FIGURE 4 | Bubble-Box results versus time including BSD, average sizes, number per time, overall volume, time period of bubble analyses, and flow rates. **(A–F)** Results for BBM-11. **(G–L)** Results for BBM-17.

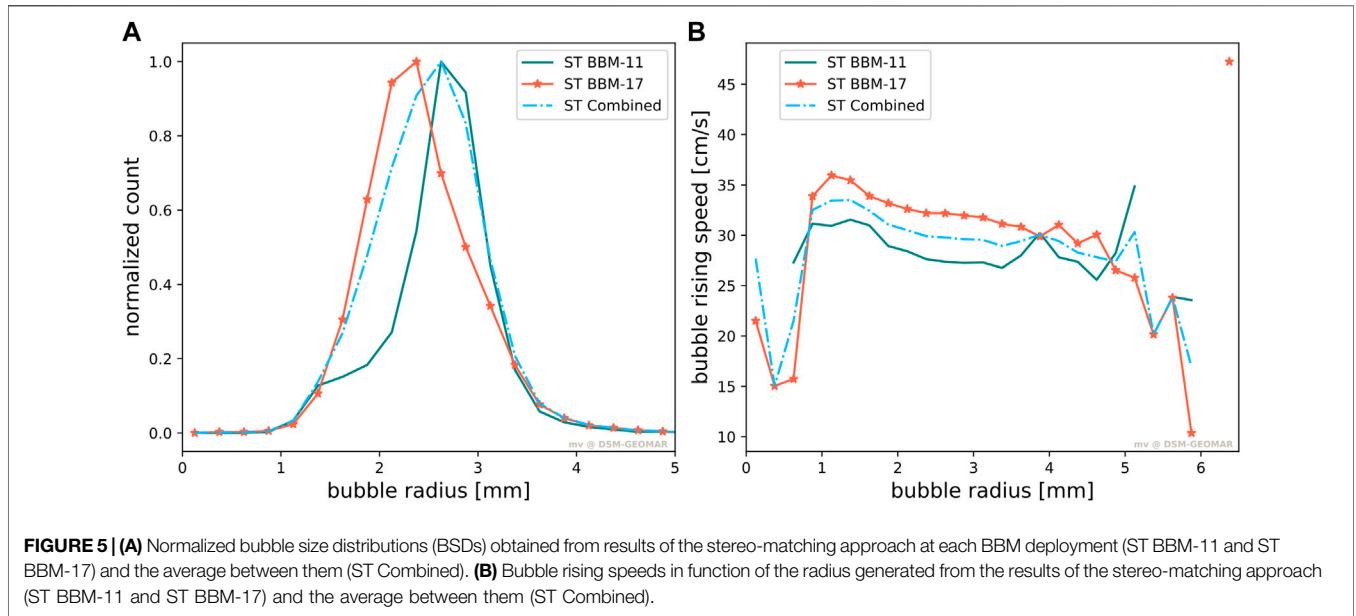


FIGURE 5 | (A) Normalized bubble size distributions (BSDs) obtained from results of the stereo-matching approach at each BBM deployment (ST BBM-11 and ST BBM-17) and the average between them (ST Combined). **(B)** Bubble rising speeds in function of the radius generated from the results of the stereo-matching approach (ST BBM-11 and ST BBM-17) and the average between them (ST Combined).

larger than 4 mm in radius scatter wider than the rising speeds of bubbles smaller than 4 mm. Rising speeds between 25 cm/s and 40 cm/s are rather rapid compared to data presented, for example, in the study by McGinnis et al. (2006), but the size distribution is very similar to many other observations from different seep locations (see discussion).

3.2 GasQuant Results

Tracking of potential seep-related acoustic anomalies in the MBES swath data resulted in eight locations for GQM-3 and

10 locations for GQM-4 (Figure 6; Supplementary Excel file F1; Supplementary Videos 3, 4). The time-series of the tracked position for each acoustic anomaly were created using the difference to the transducer position in UTM coordinates (UTM zone 11; x = easting, y = northing). The tracked seep anomaly positions were later geo-referenced using the absolute coordinate of each GasQuant deployment (Table 1) to link them accurately to the bathymetry of the study area and to each other (Figure 6). Amplitudes of each single acoustic anomaly were calculated as described in Section 2.4 (Supplementary Figures

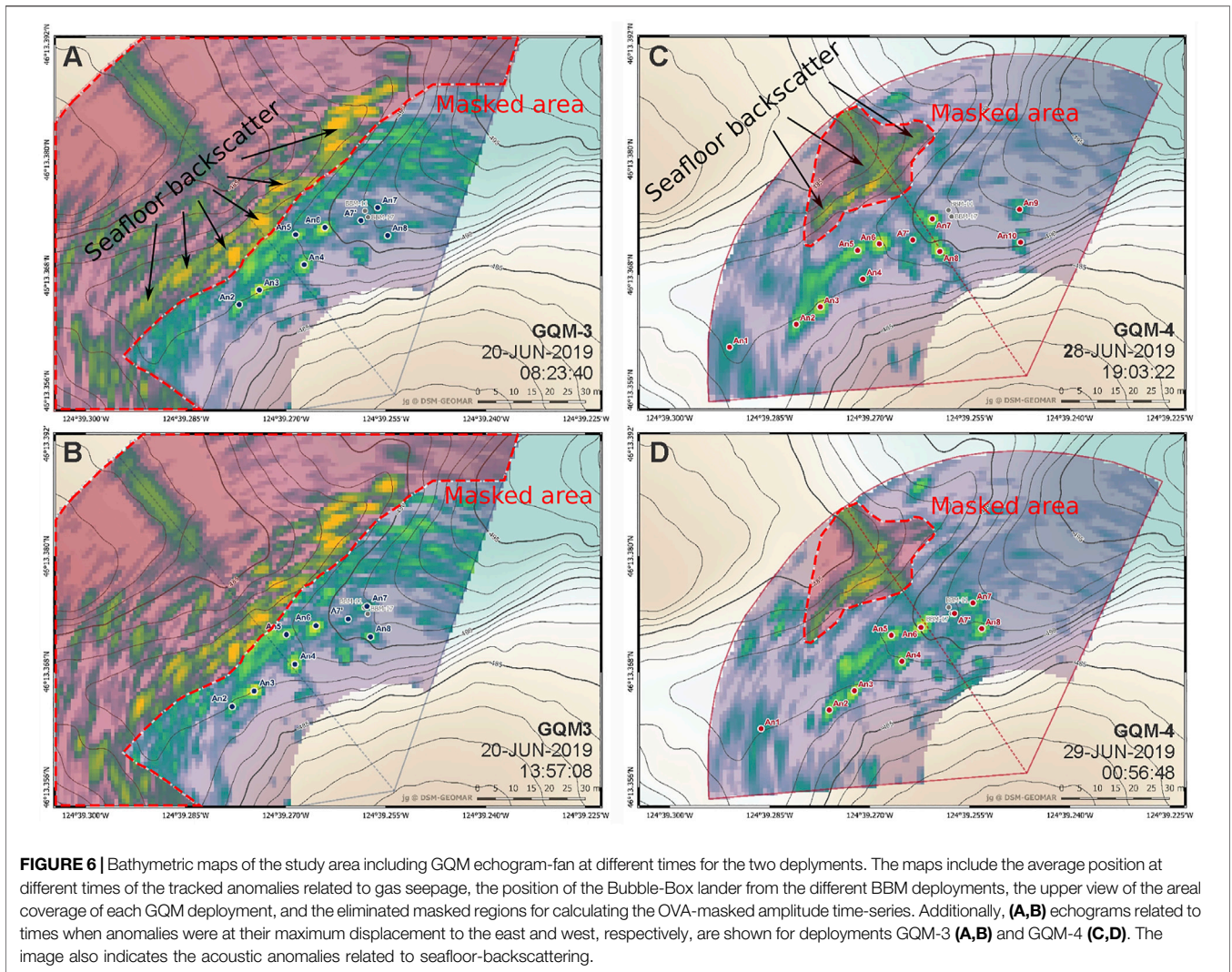


FIGURE 6 | Bathymetric maps of the study area including GQM echogram-fan at different times for the two deployments. The maps include the average position at different times of the tracked anomalies related to gas seepage, the position of the Bubble-Box lander from the different BBM deployments, the upper view of the areal coverage of each GQM deployment, and the eliminated masked regions for calculating the OVA-masked amplitude time-series. Additionally, (A,B) echograms related to times when anomalies were at their maximum displacement to the east and west, respectively, are shown for deployments GQM-3 (A,B) and GQM-4 (C,D). The image also indicates the acoustic anomalies related to seafloor-backscattering.

S7, S8; Supplementary Excel file F1). Additional strong anomalies were identified but associated to seafloor returns since they perfectly matched with the geomorphology and did not show any spatial modulation (Figure 6). Our observations indicate that GQM-3 echograms were more contaminated by seafloor backscattering than GQM-4 echograms. OVA and OVA-masked time series were calculated as indicated in Section 2.4. Masked regions containing seafloor backscattering that were excluded for the calculation of OVA-masked time series are indicated in Figure 6. Finally, the overall contribution of single anomalies was also derived for both deployments using their exponential summation (i.e., $ASA = 10 \log \sum_i 10^{Abs_{Si}/10}$). Figure 7 shows ASA, OVA, and OVA-masked time series (Figures 7B,E) together with hydrostatic pressure and ambient temperature (Figures 7A,D), and BBox results (Figures 7C,F; i.e., bubble sizes and number of bubbles per time) for comparison. For evaluating any angular dependency of the recorded backscattering, we calculated time-series of the weighted arithmetic mean of angles from the nadir of single acoustic

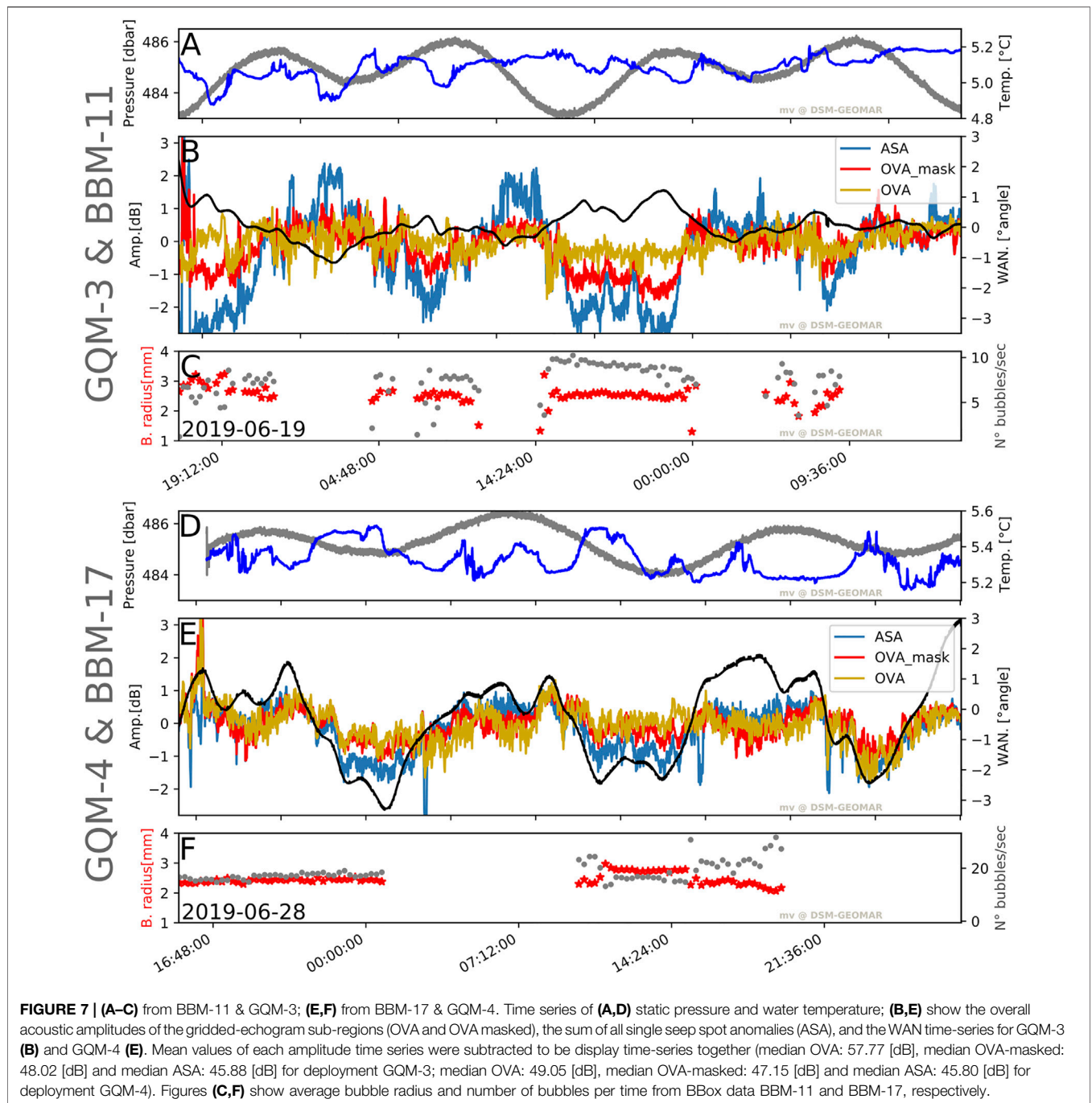
anomalies (WAN) as indicated in Eq. 13. WAN time-series are included in Figure 7.

$$WAN(t) = \frac{\sum_{i=1}^N |\varphi_i(t)| Abs_{Si}(t)}{\sum_{i=1}^N Abs_{Si}(t)} \quad (13)$$

$|\varphi_i(t)|$: Absolute angle from the nadir of each acoustic anomaly (degrees); Abs_{Si} : un-calibrated acoustical cross-section single acoustic anomaly (m^2).

3.3 Variability of Seep-Related Acoustic Anomalies

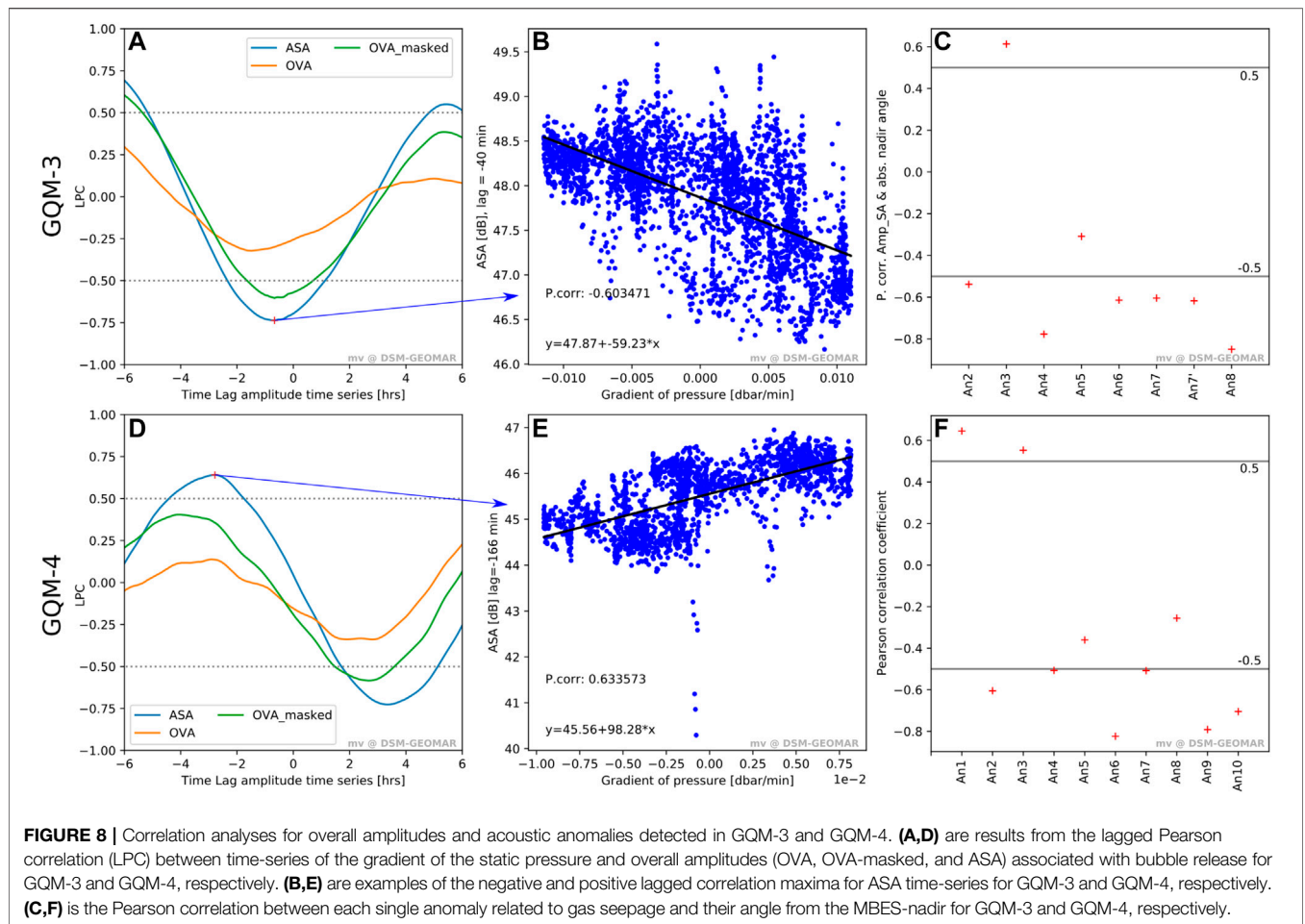
For qualitatively analyzing the bubble release variation, data were processed in the time and frequency domain. First, amplitude and position time-series were plotted jointly with the pressure time-series to visually inspect potential relationships to the tidal regimes (Figure 7; Supplementary Figures S7, S8). Seep anomaly data show a clear tide-induced lateral shift in easting



and northing of sometimes several meters with changes of the same period for most of the tracked anomalies in both deployments (from An2-An8 in GQM-3 and all the anomalies in GQM-4). Similarly, time-series from amplitudes of the total contribution of single anomalies (ASA) as well as the total amplitudes from the gridded-echogram of GQM-4 (OVA and OVA-masked) vary with a similar period as the pressure data.

For quantitatively evaluating the correlation between the acoustic amplitudes (i.e., ASA, OVA, and OVA-masked time series) and the gradient of pressure (derivative), a lagged Pearson

correlation (LPC) was performed for time lags ranging from -6 to 6 h (**Figures 8A,B,D,E**). Additionally, a simple Pearson correlation was applied between the acoustic amplitudes and the angle from the anomaly to the nadir to detect any correlation with the MBES angular response (**Figures 8C,F**). Results from the LPC show that for GQM-3 (**Figure 8A**), ASA and OVA-masked time-series have a moderate negative correlation with the pressure gradient (i.e., coefficients ≤ -0.5) whereas OVA time-series have a low negative correlation (≥ -0.5) with a small lag applied (~ -40 min for ASA and OVA-masked and ~ 90 min for



OVA). Assuming that flow rates are proportional to amplitudes, this can be interpreted as evidence of maximum flow rates increasing with the strong hydrostatic pressure decay for most of the ensouffled seeps during the GQM-3 deployment. The latter has been explained in other studies to be the result of the pressure release on the fluid conduit network and surface near gas reservoirs/pockets in the sediment (e.g., Schneider von Deimlig et al., 2010; Scandella et al., 2011; Römer et al., 2016). Furthermore, the low negative correlation between the OVA-time series and the pressure gradient can be attributed to a stronger influence of seafloor backscatter on its calculation.

LPC results for GQM-4 (Figure 9) show that the time-series amplitudes have a moderate positive correlation with pressure changes when the time lag is between ~ -3 to -2 h. This suggests that the flow rate of the overall seepage site, assuming flow rate is proportional to the amplitude, modulates in a similar way to the hydrostatic pressure. Differently than GQM-3, these results are in contradiction to the $\pi/2$ phase lag between maximum pressure and flow rate rising regimes commonly observed in other studies (Schneider von Deimlig et al., 2010).

An alternative explanation of the amplitude modulation is indicated when calculating the Pearson correlation between amplitudes of single anomalies and their relative nadir angle

(C and F in Figure 8). Results show a moderate-to-strong correlation for most of the seepage-related anomalies detected in GQM-3 (7 of 8) and GQM-4 (8 of 10). This good correlation can be interpreted as an effect of the MBES angular response or influences of additional backscattering (e.g., seafloor backscatter) captured by the main or side lobes. The latter is supported by the strong positive correlation between amplitudes (ASA, OVA, and OVA-masked) and WAN time-series observed in Figure 7E.

A Fast Fourier Transform (FFT) was applied to all amplitude and tracked position time-series to identify the main periodic components in the frequency domain (Supplementary Figure S9). Results show that for both GasQuant deployments, tracked position and amplitude time-series contain a dominant component at $\sim 0,023$ mHz (~ 12 h) as well as at $0,046$ (~ 6 h) and $0,015$ (~ 18.5 h). The latter two are recognized as harmonics; no important spectral components are recognized at higher frequencies.

3.4 Bubble-Flow Rate Strength and Variability

To obtain bubble flow rates, the scaling factor k_0 , as derived through Eq. 7, was calculated for the total contribution of

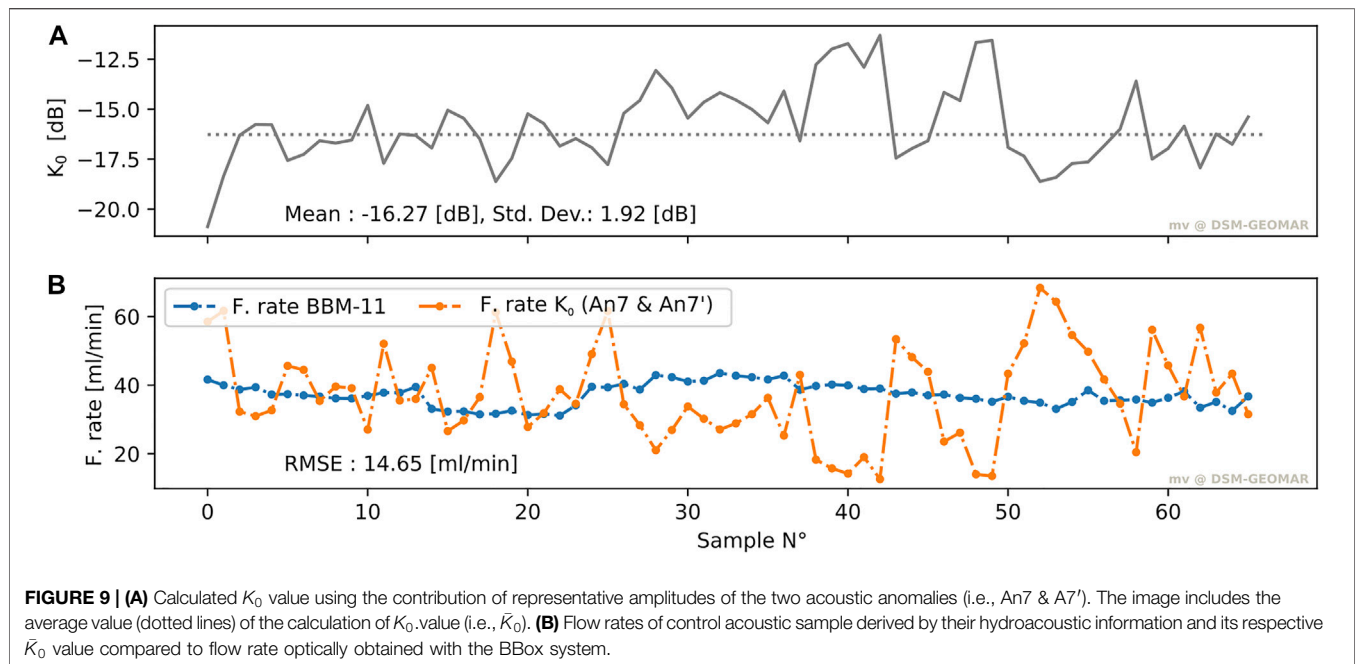


FIGURE 9 | (A) Calculated K_0 value using the contribution of representative amplitudes of the two acoustic anomalies (i.e., An7 & A7'). The image includes the average value (dotted lines) of the calculation of K_0 value (i.e., \bar{K}_0). **(B)** Flow rates of control acoustic sample derived by their hydroacoustic information and its respective \bar{K}_0 value compared to flow rate optically obtained with the BBox system.

acoustic anomalies An7 and An7' of the GQM-3 deployment (**Supplementary Figure S7**), as these were identified to jointly represent the bubble stream observed during BBM-11. This was concluded since both anomalies spatially oscillated around the reported BBox position (**Figure 6**) and it was hypothesized that these anomalies were formed by common-source bubbles horizontally separated by their sizes due to near-bottom currents when rising (see *Discussion*). As such, the k_0 value was calculated using the A_{bsTG} time-series represented by the sum of both anomalies and therefore calculated as the decibel value of their exponential summation ($A_{bsTG} = 10 \log[10^{A_{bsAn7}/10} + 10^{A_{bsAn7'}/10}]$).

The k_0 value was calculated using the optically measured numbers of bubbles N_0 per unit of time Δt for each 1-min BBox data sub-set. Subsequently, an amplitude value A_{bsTG} from the data series closest in time to each BBox observation was used for each k_0 calculation. A total of 65 data pairs could be achieved (**Figure 9A**). For finally calculating flow rates, a mean \bar{K}_0 value of -16.27 dB ($\bar{K}_0 = 10 \log \bar{k}_0$) was considered. Since bubble size variations were not significant (**Figures 4, 5**), a constant, non-modulating probability density function f_r and its associated bubble volume distribution V_r were used for deriving flow rates. A comparison between the BBox determined real flow rate (F. rate real BB) and the hydroacoustically derived ones (FC_{K0} ; **Eq. 12** and **Figure 9B**) indicates a root mean square error (RMSE) of 14.65 ml/min. For this comparison, real flow rates were calculated using the discrete functions f_r and V_r derived from results of BBM-11 deployment (mean flow rate: ~39 ml/min; **Figure 4**).

Flow rates of the entire ensonified area for each deployment were calculated using the total backscatter contribution (ASA and OVA-masked time-series). OVA time-series was not used for flow rate estimates due to the strong influence of seafloor

backscatter. Flow rates were calculated using one discrete function of f_r and V_r derived as the average from the two BBox deployments (**Figure 4**). Since the pulse length of the GasQuant was different between GQM-3 and GQM-4, it is expected that the constant of proportionality k and the scaling factor k_0 values also change. According to the definition of k in **Supplementary Eq. S.6**, the scaling factor should be theoretically multiplied by the reciprocal value of the ratio between the different pulse lengths for correction. To obtain flow rates using hydroacoustic data from GQM-4, the k_0 value was thus multiplied by 480 $\mu s/360 \mu s$ (pulse length GQM-3/pulse length GQM-4). It is uncertain if other effects occur when changing the pulse-length values of the Imagenex system. Final flow rate results are presented in **Figure 10** and average values are summarized in **Table 2**. Flow rates of the single bubble streams measured at the two different BBox deployments are included in **Figure 10** for comparison.

Since flow rates derived from the hydroacoustic data are proportional to the total acoustical backscattering cross-sections (**Eq. 12**), the flow rate variation over time is similar to the one visualized in the direct hydroacoustic information (**Figures 7B,E**). Thus, flow rates vary with the static pressures for all results in the same way as the backscattering amplitudes do. In general, we observed that flow rates derived from the OVA-masked time-series are stronger than the ones obtained from the summed contribution of the single anomalies (ASA flow rates). Mean flow results and standard deviations are similar for both deployments, including the pulse length correction. It should be noted that applying the pulse length correction amplifies the standard deviation of GQM-4 flow rate results. Small differences between flow rates of both deployments can be attributed to several possibilities that are discussed in the next section.

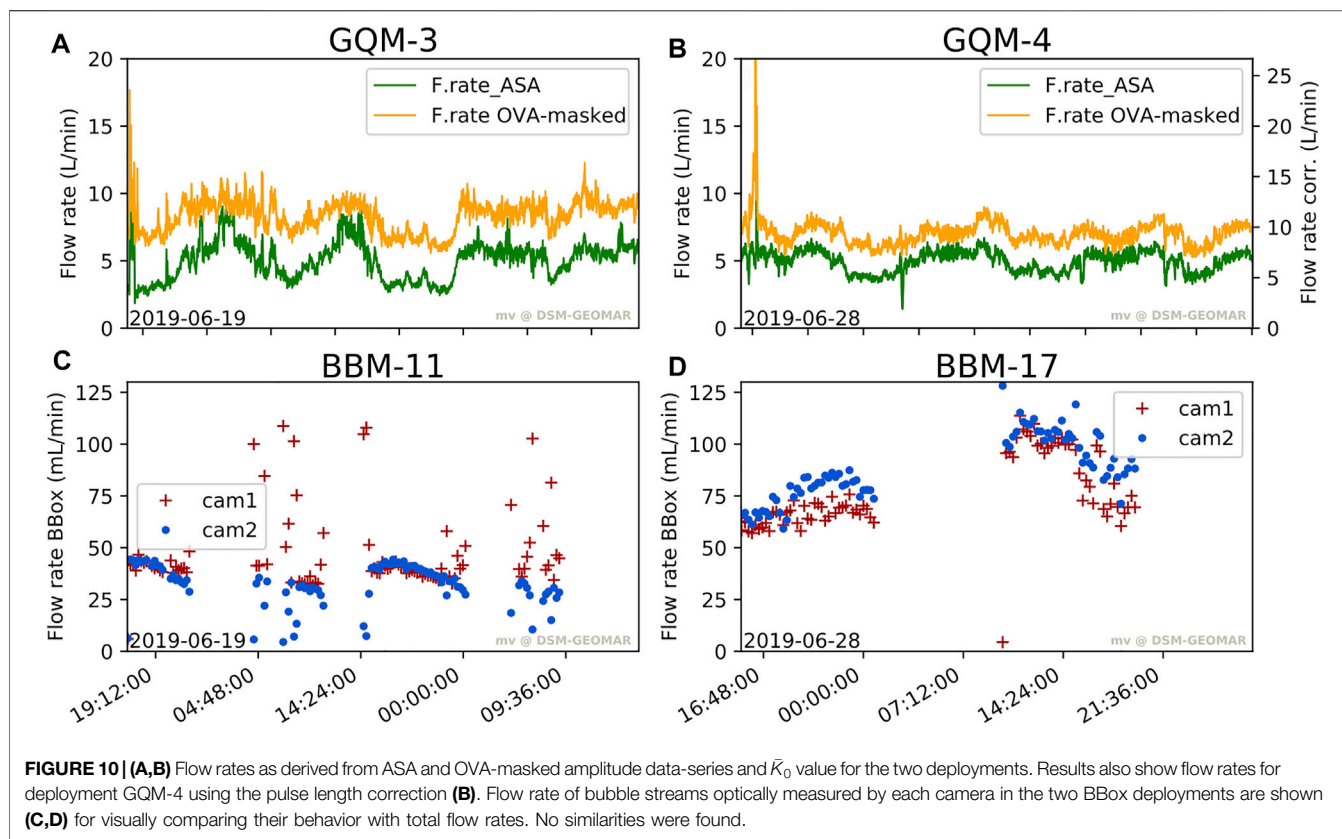


TABLE 2 | Average flow rates for deployments GQM-3 and -4 using ASA and OVA-masked time-series. The table includes flow rate values for deployment GQM-4 considering pulse length correction. Values are given in l/min, CH₄ T/yr, and CH₄ mol/yr. Standard deviation of each flow rate estimate is included.

		GQM-3			GQM-4			GQM-4 corr		
		l/min	CH ₄ T/yr (*)	\times 10 ⁶ CH ₄ mol/yr (*)	l/min	CH ₄ T/yr (*)	\times 10 ⁶ CH ₄ mol/yr (*)	l/min	CH ₄ T/yr (*)	\times 10 ⁶ CH ₄ mol/yr (*)
ASA	M. flow rate	5.04	87.46	5.45	4.982	86.41	5.39	6.642	115.21	7.18
	Std. dev.	1.44	24.90	1.55	0.799	13.85	0.86	1.065	18.47	1.15
OVA-masked	M. flow rate	8.33	144.56	9.01	7.055	122.37	7.63	9.406	163.15	10.17
	Std. dev.	1.18	20.46	1.28	1.334	23.13	1.44	1.778	30.84	1.92

(*) CH₄ density ρ_{490} : ~33 kg/m³ at 490 m water depth, considering CH₄ atmospheric density ρ_0 : ~0.66 kg/m³; Equation 17, from Veloso et al. (2015).

4 DISCUSSION

4.1 Technological Challenges and Recommendations

4.1.1 Optical Data and Processing

The described BBox lander qualifies among the accurately measuring optical lander systems for observing submarine bubble seepage as of today, due to its high sampling rate and its stereo matching approach. Its deployment imposes challenges with regard to a proper positioning of the box over the observed bubble stream (well centered and upright). If the BBox is used to provide ground-truth information for calibrating a hydroacoustic

system, the challenge increases even more because the optical bubble measurements must be linked to an identifiable acoustic location in the sonar echogram. Unlike an optical system, sonar systems are not able to differentiate bubble streams too close to each other due to the fixed beam angle and side lobes (i.e., Imagenex Delta-T system ~3° beam aperture), and therefore, an acoustic anomaly could be produced by the backscatter contribution of several bubble streams in the beam footprint (youtube-video-FK-Dive273; time video ~3:56:30; **Supplementary Figure S10**).

BBox measurements will not be ideal ground-truth information for an acoustic anomaly if the system is placed at

a location where too many bubble streams are close to each other. For calibration purposes, the BBox, or similar systems, should be deployed on isolated bubble streams. This is not always possible and a very good knowledge of the area prior the deployment is necessary. The repeated deployments of the BBox during FK190612 showed that the camera calibration must be adapted to the *in situ* conditions since the physical configuration of the BBox components did change under different temperature and pressure conditions causing slight frame deformation (see She et al., 2021). A limitation of the current BBox version is the confinement of the bubble stream within a narrow corridor and the consequences of eliminating the action of currents on bubbles in comparison to normal release. As tested by Wang and Socolofsky (2015), eliminating the interaction between bubbles and currents enhances bubble rising velocities as a result of bubble wake. Another difficulty is that the field of view can be obstructed, for example, by settling sediment or animal activity, which causes loss of information. Both difficulties are hard to prevent because the top sediment in the deep sea is typically muddy and will be stirred up when the BBox is placed on the sediment, and motile fauna will use the elevated spot of the BBox as hiding or feeding ground. Future system improvements may consider a periodical cleaning of the glass domes with a water jet to prevent sediment and animals from settling.

Observations showed that even with optimal placement of the BBox, a bubble stream drifted out of the field of view for one of the cameras. Reasons are that either the BBox tilts by slowly sinking into the sediment on one side or that the vent location below the BBox funnel changed. Future system improvements should consider increasing the field of view, adding a third camera for measurements. Additionally, the design needs to prevent the size distribution of bubbles exiting the BBox from changing due to bubble coalescence. Evidence of such coalescence was witnessed in some of the other BBox deployments, where bubbles accumulated at the top part of the box before finally leaving the box (**Supplementary Figure S4**). This will change the bubble size distribution significantly and makes the use of such data unfit for hydroacoustic calibration purposes, as these strongly depend on correct bubble size information.

4.1.2 Hydroacoustic Data and Processing

Through our hydroacoustic studies, we gained additional insight for using horizontal-looking MBESs and the Imagenex Delta-T system in particular for bubble monitoring. Since GasQuant uses a horizontal-looking MBES placed rather close to the seafloor, part of the backscattering received can be a result of the main beam and/or vertical side lobes interacting with the seafloor (**Figure 6** and **Supplementary Figure S3**), particularly if the seafloor is not flat. In the present work, a time-stacked echogram of the sonar swath was compared with the bathymetry to detect potential anomalies related to seafloor backscattering and differentiate them from seep-related anomalies that change position due to tide-dependent current changes. Results from this comparison show perfect matching between geomorphology and strong static anomalies indicating that echograms were partly

contaminated by unwanted backscattering (**Figure 6**). Researchers of future surveys might also consider vertically mapping the water column for bubble locations as, for example, Urban et al. (2022) did, using a ship-based system and then placing the GasQuant system on the seafloor to map a well-defined seep area.

As mentioned in the data quality section given in **Supplementary Section 2**, the acoustic long-term time-series relied on the *.83b files (output file Imagenex Delta-T) that contain fixed gain settings with a limited dynamic range for the amplitude. The dynamic range limitation could cause clipping of strong backscatter signals which therefore result in non-representative values of the real backscatter produced by targets (i.e., strong bubble stream). Since our approach associates acoustic backscatter with flow rates (**Eq. 12**), signal clipping would result in underestimating these flow rates. Future long-term measurements must consider storing raw data (output file from Imagenex Delta-T with extension *.837) even during long deployments to enable re-processing these data and increase the dynamic range. However, flow rate results presented here are considered to not be affected by amplitude clipping since only few percentages of the total voxel cells in gridded echograms were found to reach a common maximum (e.g., **Supplementary Figure S2**).

Finally, the two GQM deployments presented here used different pulse lengths. Theoretically, a change in pulse lengths will modify the sample volume and therefore change the amplitudes obtained from the Imagenex Delta-T since they are proportional to volume backscattering. As stated above, a theoretical correction was applied by multiplying k_0 values (scaling factor used for calculating flow rates) by the ratio between different pulse lengths. Results show that flow rates from different deployments are in agreement, including the pulse length correction (**Table 2**). However, a further investigation is needed to prove that our pulse length correction is valid to exclude additional effects when changing the pulse length parameter in the sonar settings.

4.2 Seepage-Related Results

4.2.1 Bubble Observations

Our data of 91 h of BBox observation time show, in general, no strong fluctuations in average bubble radius, the BSDs, or the amount of bubbles per time of the two individual seep spots measured. Small variation in bubble size occurs for BBM-17 (1.96 mm–3.11 mm, std. dev.: 0.23 mm), but no clear correlation to pressure changes is observed. We are convinced that the 15-min observation interval with each 1-min measuring time is sufficient to detect tide-dependent bubble size and bubble amount variations. This also holds true for the complete data set in which post-processing-related data gaps occur. In general, the 15-min measurement interval potentially can miss short-term bursts as described, for example, by Greinert (2008). Nevertheless, we think that based on the BBox data and the ROV-based observations during FK190612 that irregular and burst-like bubble release is not common in the Bubble-Alley. We are confident that the very homogenous individual observations of BBM-11 and -17 (**Figure 4**) and their almost identical bubble

size distribution (**Figure 5**) allow for deriving a general BSD probability density function, although the flow rate of the BBM-17 bubble stream is almost twice as high as that for BBM-11. Based on the rather similar and homogenous bubble size distribution (also seen during ROV-based bubble size measurements), we assume that the observed BSD can be extrapolated to calculate realistic total flow rates of the hydroacoustically investigated areas during GQM-3 and -4. For comparison, **Supplementary Figure S11** shows our BSD data together with other experimental and observational data. Even compared to other data, our measurements are rather similar (with the exception to *Muyakshin and Sauter, 2010*) pointing at the fact that the sediment properties and fluid pressure conditions at seep sites are rather similar, creating a more or less common BSD.

Bubble rising speeds show similar behavior between the two BBM deployments, although values are slightly higher in BBM-17 than BBM-11. Rising speeds between 25 cm/s and 40 cm/s (bubble radii from 1 to 5 mm; **Figure 5**) are slightly higher compared to data and models presented in other studies (e.g., *McGinnis et al., 2006; Park et al., 2017*). These results may be realistic for this seep site, although they might as well suffer from the rising speed enhancement related to bubble wake as a result of the bubble stream confinement within the BBox (*Wang and Socolofsky, 2015*). Since BRSS are directly related to our flow rate estimation, rising speed enhancement must be considered as a possible source of error in our estimates. Above a bubble radius of 4 mm, BRSS scatter wider in our measurements. This might be explainable because larger bubbles can vary more in shape and, therefore, can have different rising speeds (e.g., *Park et al., 2017*). Future analysis of BBox data could thus include shape classification (e.g., sphericity and curvature) to determine the impact of these characteristics on the bubble rising speed.

4.2.3 Spatial Distribution and Spatio-Temporal Variation of Seepage

The integration of bathymetry with geo-referenced positions of seepage occurrences identified in ROV videos (**Figure 1B**) and anomalies identified in echograms (**Figure 6**) reveals that bubble venting is concentrated along a topographic depression. The latter may be indicative of gas venting using faults as pathways before reaching the water column as suggested in other studies (e.g., *Riedel et al., 2021*). Currently, little is known about the sediment-column characteristics of the study area. Future surveys may include equipment to perform sub-bottom and seismic profiling for scanning the sediment-column and proving this hypothesis.

Acoustic results from GasQuant deployments show that spatial shifts of tracked acoustic anomalies are correlated with tide-dependent current variations (**Supplementary Figures S7, S8**), as also seen by *Crone et al. (2010)* and *Tsai et al. (2019)*. Spatial changes during GQM-4 cover larger distances which we explain by the higher swath altitude in which the GasQuant system recorded the bubbles when deployed relatively higher above the Bubble-Alley floor (see profile in **Figure 6**). The latter is strongly supported by seafloor-related anomalies in echograms that are less present in GQM-4 but also detected further upslope

when comparing their position in echograms (**Figure 6**). The absolute shift of the bubbles in 8 (GQM-3) and 11 m (GQM-4) above the seafloor is following the ENE-orientation direction of the gully, highlighting the influence of the seafloor morphology on near-bottom currents.

As suggested in **Section 3.3** (LPC analysis), the correlation between hydrostatic pressure and overall amplitude modulation (ASA and OVA-masked) provides different results for the two deployments, and the amplitude rise related to bubble flow as a result of hydrostatic pressure drops (falling tides) can only be associated to GQM-3 results. An interesting finding was that amplitudes of single acoustic anomalies and their overall contribution (ASA and OVA-masked) modulated parallel with their relative position within the echogram (**Figure 7; Supplementary Figures S7, S8**), which could be indicative of sensitivity changes of the system related to the direction (relative to the nadir) of the target. The latter is supported by the WAN time series, which can be interpreted as the relative shift from the nadir of the overall contribution of tracked single anomalies associated to bubble seepage. **Figure 7** shows that strongest fluctuations of WAN time-series are found in deployment GQM-4, and they are correlated with the overall amplitudes. From this, it is assumed that the influence of target spatial modulation is stronger in data from deployment GQM-4 than for deployment GQM-3. The angular dependency is confirmed by the experiments of *Scandella et al. (2016)* using a calibration sphere of a known acoustical backscatter cross-section, where a directional pattern was found for the Imagenex Delta-T system. This observation suggests that amplitudes collected by the sonar must be corrected by this angular dependency in order to make information from different parts of the swath comparable. Our MBES lacks proper calibration, and therefore, no angular correction was applied. Thus, the latter can be considered as a potential error in the final flux calculations.

An alternative explanation for the correlation between amplitude and anomalies' relative positions could be attributed to side-lobe effects. Because of the irregular geomorphology of the seafloor, the spatially modulated anomalies may have been differently affected by side-lobe backscatter coming from the seafloor as they move within the echogram. Unfortunately, this hypothesis cannot be tested with the data of the presented work. Future research related to quantification of bubble emissions using MBES must consider the study of MBES angular sensitivity and the overlapping of side-lobe backscattering of multiple targets in controlled environments for answering these questions. In general, our results show that amplitude correlation with hydrostatic pressure, relative position of targets, or their combination is possible. Although the reason for the amplitude variations is still not completely clear, we suggest that average values do provide a reasonable level of confidence for calculating the overall amount of gas expelled into the water column.

4.2.3 Flow Rate Quantification

One reason why stationary multibeam systems are not used regularly for quantifying gas flow rates is the difficulty of proper calibration. One approach is the experimental

calibration in a tank or ship dock as undertaken by Greinert and Nützel (2004) or Shakhova et al. (2014). Problems here lie in the generation of bubbles, the layout of the experiment, and finding the needed space to artificially generate bubbles and perform measurements without disturbing acoustic backscatter from walls and the bottom. To overcome these problems, we decided on an *in situ* calibration using a natural bubble vent, facing the challenge of finding an isolated bubble stream in the chosen AC500 seep area.

As outlined above, the two anomalies, An7 and An7', in the GQM-3 data set are most likely correlating with the bubble stream measured during BBM-11. Our best explanation is that anomalies An7 and An7' are produced by ensonifying differently sized bubbles (the BSD of BBM-11 shows more small bubbles) that come from the same vent outlet but are horizontally separated by the near-bottom currents because of their different bubble rising speeds (**Figure 11A**). Considering that the optically calculated average flow rate in BBM-11 is 0.037 L/min, a number ranging from ~135 to ~243 of such bubble streams would be needed to generate the flow rate as calculated from \bar{K}_0 (i.e., between ~5 to ~9 L/min, **Table 2**). From ROV video observations and the number of anomalies detected on the echogram, it is suggested that this scenario is plausible.

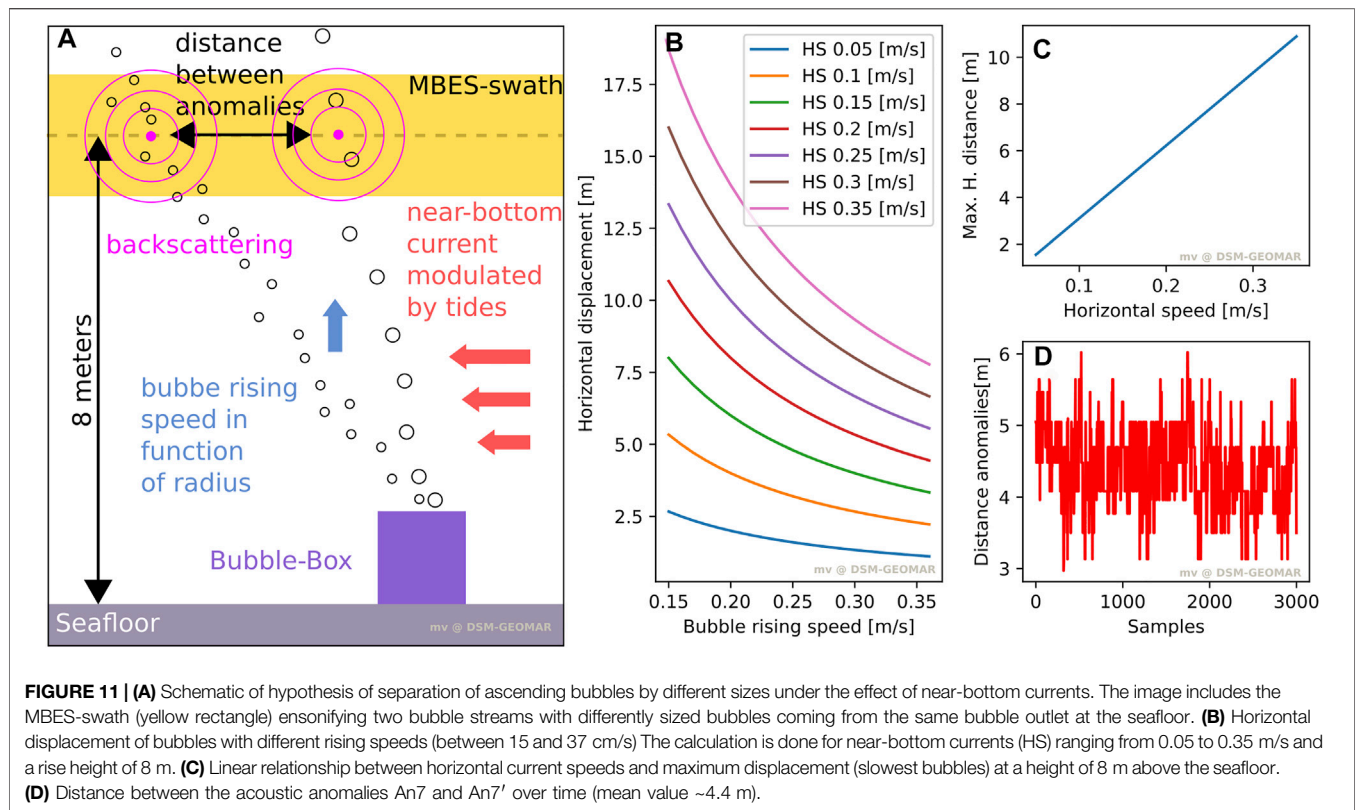
For evaluating our hypothesis, we considered common near-bottom current speeds ranging from 5 to 40 cm/s (Korgen et al., 1970), a BRS ranging from 15 to 37 cm/s (**Figure 5B**), and an observation/rise height of 8 m above the seafloor (**Figures 11A,B**). The horizontal displacement of fast and slow bubbles can be up to ~10 m (**Figure 11C**). Compared to the distance between anomalies An7 and An7' of 3–6 m (**Figure 11D**), the hypothesis of bubble separation while rising seems feasible. Alternatively, the BBM-11 measurement, if associated with a single anomaly, could only be related to An7 which is the strongest anomaly that spatially oscillates in the neighborhood of the BBox position. Mean flow rates derived from An7 are rather similar to the derived by the contribution of An7 and An7' with differences up to ~2 L/min (**Supplementary Table S4**). The rejection of An7' to be the only anomaly related to the BBox measurements is because its use for calibration would imply the obtaining of considerable large mean flow rates (up to ~63 L/min; **Supplementary Table S4**) which is something not supported by the ROV visual observations. As expected, results of the flow rates calculated from OVA-masked time-series are higher than the ones calculated from the ASA time-series since the calculation accounts for the amplitude signals of all voxels within the gridded-echogram (**Figure 10; Table 2**). Based on a simulation approach, Urban et al. (2022) suggested that the correct way of deriving the total backscatter from MBES ensonified bubbles in the water column is to use a voxel weighted mean method of all voxels in the grid area, rather than adding only the backscatter from seep-related acoustic anomalies delimited by a specific spatial domain/threshold. The latter is related to the backscattering spreading around a target voxel-neighborhood when the gridding/interpolation is applied. As such, differences between OVA-masked and ASA flow rates could be related to the use of the complete and more correct voxel-information when the OVA-masked flow rate is

calculated. On the other hand, applying this approach in real measurements with a horizontal swath close to the seafloor involves including the contribution of unwanted targets (e.g., seafloor backscatter) and noise that will influence the final flow rate result. In order to eliminate the seafloor backscatter and therefore avoid flow rate overestimation, the echogram was masked where we clearly found anomalies associated with the seafloor. Although the elimination of the main part of the unwanted backscattering is reflected in the final flow rate estimates, it is not possible to evaluate whether this effect was totally removed. Thus, the latter is an alternative explanation for the differences, although not significant (up to ~3 L/min; **Table 2**), between OVA-masked and ASA flow rates. Here, we assume that seafloor backscatter may still have an influence on the OVA-masked-based flow rate calculation, though to what extent we cannot say.

The comparison between average flow rate estimates of different deployments shows that they are similar (**Table 2**), indicating no significant release changes in time between them. Small differences, mostly reflected in OVA-masked, can be attributed to 1) a truly different flow rate fluctuation at the different times of measurements, 2) small differences of MBES areal coverage between deployments, 3) small bubble size differences between the deployments that change the backscatter response of bubbles even though real flow rates do not considerably change (**Figure 12; Supplementary Figure S6**), 4) a different deployment (i.e., GQM-3) was more affected by unwanted seafloor backscatter, or 5) the same seepage area captured by different sectors of a MBES with angular sensitivity variations. Answering which of these possibilities or a combination of some caused backscatter differences is still not possible in this study.

Using one constant BSD for obtaining flow rates over longer time from an area might always introduce an error on acoustically derived flow rate estimates as small bubble size variations over time and between bubble-vents need to be assumed. **Figure 12** illustrates how sensitive the used hydroacoustic inversion method (**Eq. 11**) is to BSD shifts. Flow rate changes considerably even for small shifts of the mode of the BSD (flow rate increases almost 10 times when the BSD mode shifts from a radius of 2 mm to 3 mm). For a more stable acoustical response associated with bubble sizes, a system that operates at a lower frequency (e.g., 38 kHz) would have been the better choice for the observed bubble size distribution and water depth. However, using a lower frequency demands a larger transducer to keep the same beam resolution which increases the weight and power consumption of the system, making it harder to be deployed by an ROV in the undertaken agile and simple way.

In general, flow rate results of the Bubble-Alley of the AC500 site (in l/min and CH₄ tones/year) are similar to others reported in the literature, for example, from the Black Sea, the Cascadia Margin, or the North Sea (**Supplementary Table S5**) and stands for a well active, natural seep area. The remaining uncertainties of our quantification are well within the range of other uncertainties, particularly when considering spatial assumptions and the extrapolation of a few directly measured seep vents, which are then extrapolated to entire areas (e.g., Römer et al., 2012).



5 SUMMARY AND CONCLUSION

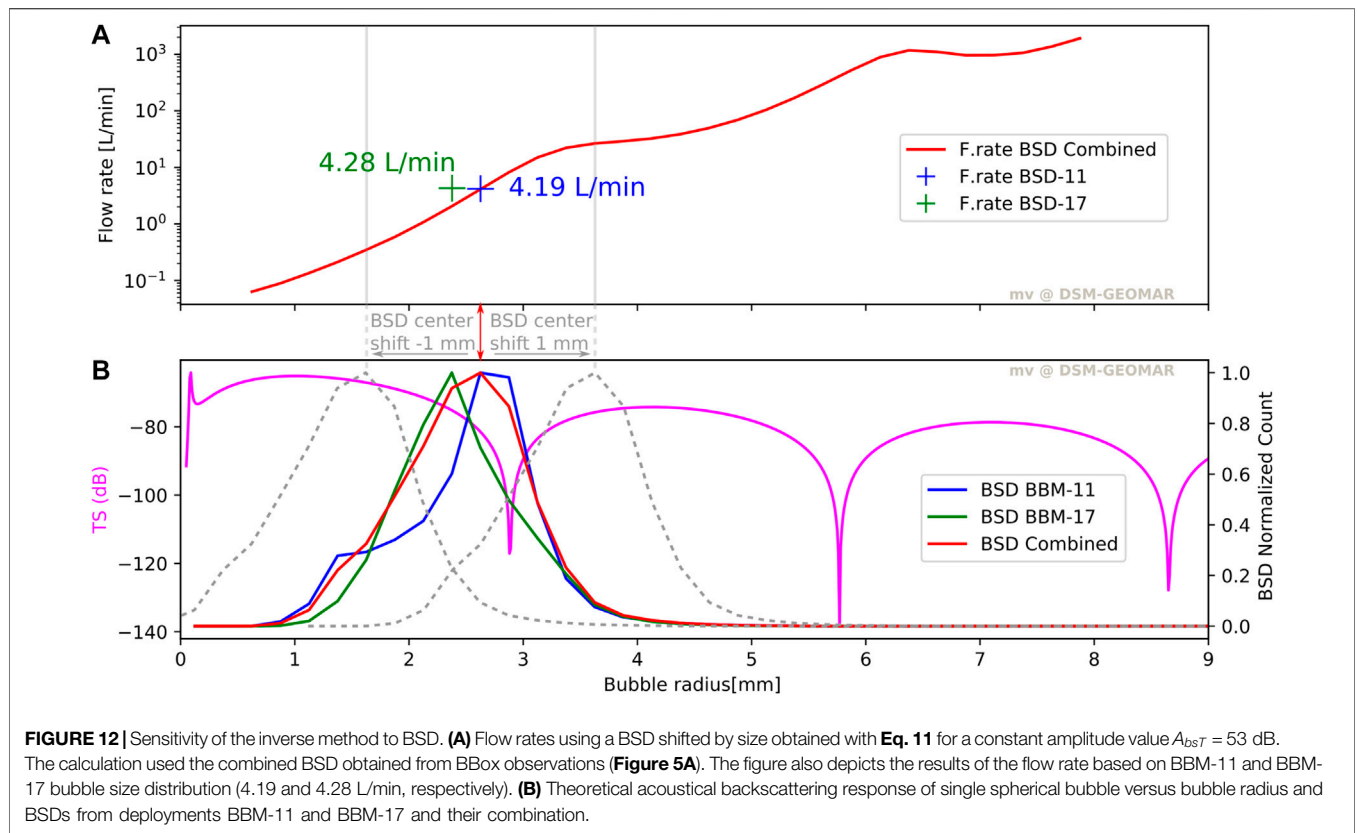
In this study, we evaluated an *in situ* experimental setup which consisted of an acoustic multibeam system (GasQuant-II) and a stereo camera system (Bubble-Box) deployed in tandem. This sensor configuration was chosen for 1) calibrating the hydroacoustic system using optical information for estimating bubble flow-rates and 2) quantitatively assessing the temporal and spatial release activity of the seepage site. To achieve 1) and 2), we first proposed a method for bubble flow rate quantification using echo-grid integration of seepage-related MBES backscatter and simultaneous optical information of bubble release. This method was applied on a dataset acquired during the cruise FK190612 with RV FALKOR at the Astoria Canyon site AC500 (Bubble-Alley).

From a technical perspective, we concluded that using BBox measurements for *in situ* calibration of a horizontal-looking MBES is possible but imposes challenges regarding the box positioning over an isolated bubble-stream that at the same time can be individually detected in acoustic images. The selected bubble stream used for calibration in this experiment was partially influenced by acoustic returns from close-by bubble streams. Future surveys that attempt to use a similar sensor setup are advised to gain prior knowledge regarding the spatial distribution of the seeps, for example, using AUV-based high-resolution down-looking MBES surveys. These surveys could help with identifying and eliminating seafloor-related backscatter which was surprisingly difficult to differentiate from bubble-related backscattering in this experiment. Our

results show that eliminating strong seafloor-related backscatter is crucial to avoid flow rate overestimation using the presented inverse method.

Our evaluation exposes a number of limitations of the current measurement design, therefore providing directions for future improvements of this system. One of them is the dynamic range limitation associated with the recorded 0.83b files. Future improvement of the system must take care that the 0.837 raw data files are also properly stored even when data acquisition is performed during longer periods of time. Additionally, our results suggest a possible relationship between backscatter amplitudes and relative positions of acoustic anomalies. A calibration experiment is necessary to equalize the sensitivity for the different beam angles (relative calibration). Additionally, we hypothesize that correlation of amplitude with anomalies' relative position could also be caused by seafloor-backscatter (from main and side lobes) that overlaps differently with the tracked-acoustic anomaly as it moves within the echogram-fan. Furthermore, we cannot exclude that the measured acoustic backscattering strength was influenced by modifying the MBES range setting between dives which influenced the acoustic pulse length of our measurements. Future investigations using the GasQuant II system should either take more care to use the same setup or calibrate different settings against each other using the exact same target.

From a scientific point of view, our BBox results do not show strong fluctuations of bubble size, BRSS, and flow rates, suggesting that emissions are relatively stable and constant at the study area. BSDs are similar between the two observed bubble streams, and



therefore, we assume a general BSD for the entire area. Additionally, BSD is similar to published data from other areas pointing out that the sediment properties and fluid pressure conditions at seep sites are rather similar. The measured BRSs for the study area are slightly higher compared to values from published data and models. BRS values might be realistic for the study area but could alternatively be explained to be the result of the elimination of the interaction between currents and bubbles, which is produced by the bubble stream confinement within the BBox. This thus represents a possible source of error in our flow rate estimates.

The analysis of the spatial seep distribution shows that seeps are clustered along a topographic depression, which may suggest that faults are used as gas-migrating pathways. Sediment-column profiles are required to prove this hypothesis.

The spatiotemporal analysis of acoustic anomalies tracked in the echograms of the two deployments reveal that bubble streams are spatially modulated by near-bottom currents associated with the tidal regime. On the other hand, only overall backscattering amplitudes from GQM-3 can be associated with the rise in bubble-flow resulting from falling tides as observed in other studies. Due to the uncertainty caused by the MBES angular sensitivity, it was not possible to establish a precise amplitude-tide relationship. Despite this relative calibration error, the average flow rate results can be used to represent a realistic amount of gas expelled into the water column. In comparison with other studies, our results indicate that the

flow rates presented in this work ranging from 5.38×10^6 to 9.01×10^6 CH₄ mol/year can be categorized as a well active natural seep area.

It has to be noted that the presented work is one of the few existing attempts of calibrating MBES using simultaneous optical measurements. We believe that the results presented here provide insightful information regarding the method for calibrating MBES with simultaneous optical information *in situ*, as well as indicating the challenges, the problems, and their possible solutions. Future studies related to MBES-optical sensor configuration using the presented method must address the issues and consider the recommendations presented in this work for improving the precision of gas flow evaluations.

DATA AVAILABILITY STATEMENT

The original contributions presented in the study are included in the article/Supplementary Material; further inquiries can be directed to the corresponding author.

AUTHOR CONTRIBUTIONS

The present work can be subdivided in different contributions related to 1) the development of the GasQuant-II and Bubble Box system, 2) their use during cruise FK190612, 3) planning the

research in the field and supplying financial support, 4) elaboration of methodology for GasQuant data post-processing, 5) GasQuant data post-processing, 6) elaboration of methodology for BBox data post-processing, 7) BBox data post-processing, 8) data analysis and elaboration of hypotheses, and 9) interpretation and discussion of results. In detail, MV-A contributed to 4, 5, 7, 8, and 9; PU contributed to 1, 4, 8, and 9; TW contributed to 1, 2, and 3; KK contributed to 1, 6, and 9; MS contributed to 6, 7, 8, and 9; and JG contributed to 1, 2, 3, 4, 6, 8, and 9. The manuscript was written by MV-A and JG with contributions of all authors.

FUNDING

Cruise FK190612 was funded by the Schmidt Ocean Institute as part of the “Observing seafloor methane seepage at the edge of hydrate stability,” based on a proposal formulated under the leadership of the Gas Hydrates and Benthic Ecology projects at the United States Geological Survey (USGS). Funding for cruise preparations, travel, and article writing for TW, JG, and MV-A came through GEOMAR internal funds from the Deep Sea Monitoring group. Incidental cruise support was provided through interagency agreement DE-FE0023495 between the USGS and the United States Department of Energy for gas hydrate research.

REFERENCES

- Ainslie, M. A., and Leighton, T. G. (2009). Near Resonant Bubble Acoustic Cross-Section Corrections, Including Examples from Oceanography, Volcanology, and Biomedical Ultrasound. *J. Acoust. Soc. Am.* 126, 2163–2175. doi:10.1121/1.3180130
- Ainslie, M. A., and Leighton, T. G. (2011). Review of Scattering and Extinction Cross-Sections, Damping Factors, and Resonance Frequencies of a Spherical Gas Bubble. *J. Acoust. Soc. Am.* 130, 3184–3208. doi:10.1121/1.3628321
- Baumberger, T., Embley, R. W., Merle, S. G., Lilley, M. D., Raineault, N. A., and Lupton, J. E. (2018). Mantle-Derived Helium and Multiple Methane Sources in Gas Bubbles of Cold Seeps along the Cascadia Continental Margin. *Geochem. Geophys. Geosyst.* 19, 4476–4486. doi:10.1029/2018GC007859
- Bergès, B. J. P., Leighton, T. G., and White, P. R. (2015). Passive Acoustic Quantification of Gas Fluxes during Controlled Gas Release Experiments. *Int. J. Greenh. Gas Control* 38, 64–79. doi:10.1016/j.ijggc.2015.02.008
- Berndt, C., Feseker, T., Treude, T., Krastel, S., Liebetrau, V., Niemann, H., et al. (2014). Temporal Constraints on Hydrate-Controlled Methane Seepage off Svalbard. *Science* 343, 284–287. doi:10.1126/science.1246298
- Boetius, A., Ravenschlag, K., Schubert, C. J., Rickert, D., Widdel, F., Gieseke, A., et al. (2000). A Marine Microbial Consortium Apparently Mediating Anaerobic Oxidation of Methane. *Nature* 407, 623–626. doi:10.1038/35036572
- Campbell, K. A. (2006). Hydrocarbon Seep and Hydrothermal Vent Paleoenvironments and Paleontology: Past Developments and Future Research Directions. *Palaeogeogr. Palaeoclimatol. Palaeoecol.* 232, 362–407. doi:10.1016/j.palaeo.2005.06.018
- Caudron, C., Vandemeulebrouck, J., and Sohn, R. A. (2022). Turbulence-induced Bubble Nucleation in Hydrothermal Fluids beneath Yellowstone Lake. *Commun. Earth Environ.* 3, 1–6. doi:10.1038/s43247-022-00417-6
- Crone, T. J., Wilcock, W. S. D., and McDuff, R. E. (2010). Flow Rate Perturbations in a Black Smoker Hydrothermal Vent in Response to a Mid-ocean Ridge Earthquake Swarm. *Geochem. Geophys. Geosyst.* 11, 13. doi:10.1029/2009GC002926
- De Leo, F. C., Ogata, B., Sastri, A. R., Heesemann, M., Mihály, S., Galbraith, M., et al. (2018). High-frequency Observations from a Deep-Sea Cabled

ACKNOWLEDGMENTS

We thank the Schmidt Ocean Institute (SOI) for providing access to the *R/V Falkor* and are grateful to SOI's staff, the ship's crew, and the operators of *ROV SuBastian* for their professionalism and support that made this cruise a success. Our gratitude to C. Ruppel (USGS) for the opportunity to participate in the cruise and to A. Demopoulos for her outstanding at-sea leadership. E. Suess, B. Collier, and Jonathan Fram from Oregon State, as well as H. Mendlovitz (UNC), provided support for peripherals and logistics necessary for GasQuant and the BBox. We further want to thank the rest of the scientific party and ship's crew for the relaxed and professional work environment during the cruise. Special thanks go to B. Scandella for kindly discussing results of his publications with us. Finally, we would like to thank the reviewers for their comments and suggestions, which helped us to improve the quality of the manuscript. This is publication 56 of the DeepSea Monitoring group at GEOMAR.

SUPPLEMENTARY MATERIAL

The Supplementary Material for this article can be found online at: <https://www.frontiersin.org/articles/10.3389/feart.2022.858992/full#supplementary-material>

- Observatory Reveal Seasonal Overwintering of *Neocalanus* Spp. In Barkley Canyon, NE Pacific: Insights into Particulate Organic Carbon Flux. *Prog. Oceanogr.* 169, 120–137. doi:10.1016/j.pocean.2018.06.001
- Doya, C., Chatzievangelou, D., Bahamon, N., Purser, A., De Leo, F. C., Juniper, S. K., et al. (2017). Seasonal Monitoring of Deep-Sea Megabenthos in Barkley Canyon Cold Seep by Internet Operated Vehicle (IOV). *PLOS ONE* 12, e0176917. doi:10.1371/journal.pone.0176917
- Etiopie, G. (2009). Natural Emissions of Methane from Geological Seepage in Europe. *Atmos. Environ.* 43, 1430–1443. doi:10.1016/j.atmosenv.2008.03.014
- Francois, R. E., and Garrison, G. R. (1982). Sound Absorption Based on Ocean Measurements. Part II: Boric Acid Contribution and Equation for Total Absorption. *J. Acoust. Soc. Am.* 72, 1879–1890. doi:10.1121/1.388673
- Greinert, J., Bohrmann, G., and Suess, E. (2001). “Gas Hydrate-Associated Carbonates and Methane-Venting at Hydrate Ridge: Classification, Distribution, and Origin of Authigenic Lithologies,” in *Natural Gas Hydrates: Occurrence, Distribution, and Detection* (Washington, DC: American Geophysical Union AGU), 99–113. doi:10.1029/GM124p0099
- Greinert, J. (2008). Monitoring Temporal Variability of Bubble Release at Seeps: The Hydroacoustic Swath System GasQuant. *J. Geophys. Res.* 113, 7048. doi:10.1029/2007JC004704
- Greinert, J., and Nützel, B. (2004). Hydroacoustic Experiments to Establish a Method for the Determination of Methane Bubble Fluxes at Cold Seeps. *Geo-Marine Lett.* 24, 75–85. doi:10.1007/s00367-003-0165-7
- Higgs, B., Mountjoy, J. J., Crutchley, G. J., Townend, J., Ladroit, Y., Greinert, J., et al. (2019). Seep-bubble Characteristics and Gas Flow Rates from a Shallow-Water, High-Density Seep Field on the Shelf-To-Slope Transition of the Hikurangi Subduction Margin. *Mar. Geol.* 417, 105985. doi:10.1016/j.margeo.2019.105985
- Jerram, K., Weber, T. C., and Beaudoin, J. (2015). Split-beam Echo Sounder Observations of Natural Methane Seep Variability in the Northern Gulf of Mexico. *Geochem. Geophys. Geosyst.* 16, 736–750. doi:10.1002/2014GC005429
- Kannberg, P. K., Tréhu, A. M., Pierce, S. D., Paull, C. K., and Caress, D. W. (2013). Temporal Variation of Methane Flares in the Ocean above Hydrate Ridge, Oregon. *Earth Planet. Sci. Lett.* 368, 33–42. doi:10.1016/j.epsl.2013.02.030
- Kirschke, S., Bousquet, P., Ciais, P., Saunoy, M., Canadell, J. G., Dlugokencky, E. J., et al. (2013). Three Decades of Global Methane Sources and Sinks. *Nat. Geosci.* 6, 813–823. doi:10.1038/ngeo1955

- Korgen, B. J., Bodvarsson, G., and Kulm, L. D. (1970). Current Speeds Near the Ocean Floor West of Oregon. *Deep Sea Res. Oceanogr. Abstr.* 17, 353–357. doi:10.1016/0011-7471(70)90026-4
- Leifer, I., and Boles, J. (2005). Turbine Tent Measurements of Marine Hydrocarbon Seeps on Subhourly Timescales. *J. Geophys. Res.* 110, 12. doi:10.1029/2003JC002207
- Leifer, I., Chernykh, D., Shakhova, N., and Semiletov, I. (2017). Sonar Gas Flux Estimation by Bubble Insonification: Application to Methane Bubble Flux from Seep Areas in the Outer Laptev Sea. *Cryosphere* 11, 1333–1350. doi:10.5194/tc-11-1333-2017
- Leifer, I., and Culling, D. (2010). Formation of Seep Bubble Plumes in the Coal Oil Point Seep Field. *Geo-Mar Lett.* 30, 339–353. doi:10.1007/s00367-010-0187-x
- Leifer, I., Patro, R. K., and Bowyer, P. (2000). A Study on the Temperature Variation of Rise Velocity for Large Clean Bubbles. *J. Atmos. Ocean. Technol.* 17, 1392–1402. doi:10.1175/1520-0426(2000)017<1392:asottv>2.0.co;2
- Levin, L. A., Baco, A. R., Bowden, D. A., Colaco, A., Cordes, E. E., Cunha, M. R., et al. (2016). Hydrothermal Vents and Methane Seeps: Rethinking the Sphere of Influence. *Front. Mar. Sci.* 3, 72. doi:10.3389/fmars.2016.00072
- Li, J., Roche, B., Bull, J. M., White, P. R., Davis, J. W., Deponte, M., et al. (2020a). Passive Acoustic Monitoring of a Natural CO₂ Seep Site - Implications for Carbon Capture and Storage. *Int. J. Greenh. Gas Control* 93, 102899. doi:10.1016/j.ijggc.2019.102899
- Li, J., Roche, B., Bull, J. M., White, P. R., Leighton, T. G., Provenzano, G., et al. (2020b). Broadband Acoustic Inversion for Gas Flux Quantification-Application to a Methane Plume at Scanner Pockmark, Central North Sea. *J. Geophys. Res. Oceans* 125, 21. e2020JC016360. doi:10.1029/2020JC016360
- Liebetrau, V., Eisenhauer, A., and Linke, P. (2010). Cold Seep Carbonates and Associated Cold-Water Corals at the Hikurangi Margin, New Zealand: New Insights into Fluid Pathways, Growth Structures and Geochronology. *Mar. Geol.* 272, 307–318. doi:10.1016/j.margeo.2010.01.003
- Longo, M., Lazzaro, G., Caruso, C. G., Radulescu, V., Radulescu, R., Sciré Scappuzzo, S. S., et al. (2021). Black Sea Methane Flares from the Seafloor: Tracking Outgassing by Using Passive Acoustics. *Front. Earth Sci.* 9, 678834. doi:10.3389/feart.2021.678834
- McGinnis, D. F., Greinert, J., Artemov, Y., Beaubien, S. E., and Wüest, A. (2006). Fate of Rising Methane Bubbles in Stratified Waters: How Much Methane Reaches the Atmosphere? *J. Geophys. Res.* 111, C09007. doi:10.1029/2005JC003183
- Muyakshin, S. I., and Sauter, E. (2010). The Hydroacoustic Method for the Quantification of the Gas Flux from a Submersed Bubble Plume. *Oceanol.* 50 (6), 1001. doi:10.1134/S0001437010060202
- Nikolovska, A., Sahling, H., and Bohrmann, G. (2008). Hydroacoustic Methodology for Detection, Localization, and Quantification of Gas Bubbles Rising from the Seafloor at Gas Seeps from the Eastern Black Sea. *Geochem. Geophys. Geosyst.* 9, 10010. doi:10.1029/2008GC002118
- Park, S. H., Park, C., Lee, J., and Lee, B. (2017). A Simple Parameterization for the Rising Velocity of Bubbles in a Liquid Pool. *Nucl. Eng. Technol.* 49, 692–699. doi:10.1016/j.net.2016.12.006
- Pohlman, J. W., Greinert, J., Ruppel, C., Silyakova, A., Vielstädte, L., Casso, M., et al. (2017). Enhanced CO₂ Uptake at a Shallow Arctic Ocean Seep Field Overwhelms the Positive Warming Potential of Emitted Methane. *Proc. Natl. Acad. Sci. U.S.A.* 114, 5355–5360. doi:10.1073/pnas.1618926114
- Razaz, M., Di Iorio, D., Wang, B., and MacDonald, I. (2020). Temporal Variations of a Natural Hydrocarbon Seep Using a Deep-Sea Camera System. *J. Atmos. Ocean. Technol.* 37, 1737–1751. doi:10.1175/JTECH-D-19-0137.1
- Rehder, G., Brewer, P. W., Peltzer, E. T., and Friederich, G. (2002). Enhanced Lifetime of Methane Bubble Streams within the Deep Ocean. *Geophys. Res. Lett.* 29, 21-1-21-4. doi:10.1029/2001GL013966
- Rehder, G., Leifer, I., Brewer, P., Friederich, G., and Peltzer, E. T. (2009). Controls On Methane Bubble Dissolution Inside And Outside The Hydrate Stability Field From Open Ocean Field Experiments And Numerical Modeling. *Marine Chem.* 114 (1-2), 19–30. doi:10.1016/j.marchem.2009.03.004
- Riedel, M., Hähnel, L., Bialas, J., Bachmann, A. K., Gaide, S., Wintersteller, P., et al. (2021). Controls on Gas Emission Distribution on the Continental Slope of the Western Black Sea. *Front. Earth Sci.* 8, 601254. doi:10.3389/feart.2020.601254
- Riedel, M., Scherwath, M., Römer, M., Veloso, M., Heesemann, M., and Spence, G. D. (2018). Distributed Natural Gas Venting Offshore along the Cascadia Margin. *Nat. Commun.* 9, 3264. doi:10.1038/s41467-018-05736-x
- Römer, M., Riedel, M., Scherwath, M., Heesemann, M., and Spence, G. D. (2016). Tidally Controlled Gas Bubble Emissions: A Comprehensive Study Using Long-Term Monitoring Data from the NEPTUNE Cabled Observatory Offshore Vancouver Island. *Geochem. Geophys. Geosyst.* 17, 3797–3814. doi:10.1002/2016GC006528
- Römer, M., Sahling, H., Pape, T., Bahr, A., Feseker, T., Wintersteller, P., et al. (2012). Geological Control and Magnitude of Methane Ebullition from a High-Flux Seep Area in the Black Sea-The Kerch Seep Area. *Mar. Geol.* 319-322, 57–74. doi:10.1016/j.margeo.2012.07.005
- Römer, M., Wenau, S., Mau, S., Veloso, M., Greinert, J., Schlüter, M., et al. (2017). Assessing Marine Gas Emission Activity and Contribution to the Atmospheric Methane Inventory: A Multidisciplinary Approach from the Dutch Dogger Bank Seep Area (North Sea). *Geochem. Geophys. Geosyst.* 18, 2617–2633. doi:10.1002/2017GC006995
- Ruppel, C. D., and Kessler, J. D. (2017). The Interaction of Climate Change and Methane Hydrates. *Rev. Geophys.* 55, 126–168. doi:10.1002/2016RG000534
- Sahling, H., Bohrmann, G., Artemov, Y. G., Bahr, A., Brüning, M., Klapp, S. A., et al. (2009). Vodyanitskii Mud Volcano, Sorokin Trough, Black Sea: Geological Characterization and Quantification of Gas Bubble Streams. *Mar. Petroleum Geol.* 26, 1799–1811. doi:10.1016/j.marpetgeo.2009.01.010
- Sahling, H., Rickert, D., Lee, R., Linke, P., and Suess, E. (2002). Macrofaunal Community Structure and Sulfide Flux at Gas Hydrate Deposits from the Cascadia Convergent Margin, NE Pacific. *Mar. Ecol. Prog. Ser.* 231, 121–138. doi:10.3354/meps231121
- Sarkar, K., and Prosperetti, A. (1993). Coherent and Incoherent Scattering from Oceanic Bubbles. *J. Acoust. Soc. Am.* 93, 2379. doi:10.1121/1.406101
- Sauter, E. J., Muyakshin, S. I., Charlou, J.-L., Schlüter, M., Boetius, A., Jerosch, K., et al. (2006). Methane Discharge from a Deep-Sea Submarine Mud Volcano into the Upper Water Column by Gas Hydrate-Coated Methane Bubbles. *Earth Planet. Sci. Lett.* 243, 354–365. doi:10.1016/j.epsl.2006.01.041
- Scandella, B. P., Pillsbury, L., Weber, T., Ruppel, C., Hemond, H. F., and Juanes, R. (2016). Ephemerality of Discrete Methane Vents in Lake Sediments. *Geophys. Res. Lett.* 43, 4374–4381. doi:10.1002/2016GL068668
- Scandella, B. P., Varadharajan, C., Hemond, H. F., Ruppel, C., and Juanes, R. (2011). A Conduit Dilation Model of Methane Venting from Lake Sediments. *Geophys. Res. Lett.* 38, 6. doi:10.1029/2011GL046768
- Schmale, O., Leifer, I., Deimling, J. S. v., Stolle, C., Krause, S., Kießlich, K., et al. (2015). Bubble Transport Mechanism: Indications for a Gas Bubble-Mediated Inoculation of Benthic Methanotrophs into the Water Column. *Cont. Shelf Res.* 103, 70–78. doi:10.1016/j.csr.2015.04.022
- Schneider von Deimling, J., Greinert, J., Chapman, N. R., Rabbal, W., and Linke, P. (2010). Acoustic Imaging of Natural Gas Seepage in the North Sea: Sensing Bubbles Controlled by Variable Currents. *Limnol. Oceanogr. Methods* 8, 155–171. doi:10.4319/lom.2010.8.155
- Schneider von Deimling, J., Rehder, G., Greinert, J., McGinnis, D. F., Boetius, A., and Linke, P. (2011). Quantification of Seep-Related Methane Gas Emissions at Tommeliten, North Sea. *Cont. Shelf Res.* 31, 867–878. doi:10.1016/j.csr.2011.02.012
- Shakhova, N., Semiletov, I., Leifer, I., Sergienko, V., Salyuk, A., Kosmach, D., et al. (2014). Ebullition and Storm-Induced Methane Release from the East Siberian Arctic Shelf. *Nat. Geosci.* 7, 64–70. doi:10.1038/ngeo2007
- Shakhova, N., Semiletov, I., Salyuk, A., Yusupov, V., Kosmach, D., and Gustafsson, Ö. (2010). Extensive Methane Venting to the Atmosphere from Sediments of the East Siberian Arctic Shelf. *Science* 327, 1246–1250. doi:10.1126/science.1182221
- She, M., Song, Y., Mohrmann, J., and Köser, K. (2019). “Adjustment and Calibration of Dome Port Camera Systems for Underwater Vision,” in *Pattern Recognition Lecture Notes in Computer Science*. Editors G. A. Fink, S. Frintrop, and X. Jiang (Cham: Springer International Publishing), 79–92. doi:10.1007/978-3-030-33676-9_6
- She, M., Weiß, T., Song, Y., Urban, P., Greinert, J., and Köser, K. (2022). Marine Bubble Flow Quantification Using Wide-Baseline Stereo Photogrammetry. *ISPRS J. Photogrammet. Remo. Sens.*
- Skarke, A., Ruppel, C., Kodis, M., Brothers, D., and Lobecker, E. (2014). Widespread Methane Leakage from the Sea Floor on the Northern US Atlantic Margin. *Nat. Geosci.* 7, 657–661. doi:10.1038/ngeo2232
- Smith, A. J., Mienert, J., Bünz, S., and Greinert, J. (2014). Thermogenic Methane Injection via Bubble Transport into the Upper Arctic Ocean from the Hydrate-

- Charged Vestnesa Ridge, Svalbard. *Geochem. Geophys. Geosyst.* 15, 1945–1959. doi:10.1002/2013GC005179
- Suess, E. (2014). Marine Cold Seeps and Their Manifestations: Geological Control, Biogeochemical Criteria and Environmental Conditions. *Int. J. Earth Sci. Geol. Rundsch* 103, 1889–1916. doi:10.1007/s00531-014-1010-0
- Suess, E., Torres, M. E., Bohrmann, G., Collier, R. W., Greinert, J., Linke, P., et al. (1999). Gas Hydrate Destabilization: Enhanced Dewatering, Benthic Material Turnover and Large Methane Plumes at the Cascadia Convergent Margin. *Earth Planet. Sci. Lett.* 170, 1–15. doi:10.1016/S0012-821X(99)00092-8
- Thuraisingham, R. A. (1997). New Expressions of Acoustic Cross-Sections of a Single Bubble in the Monopole Bubble Theory. *Ultrasonics* 35, 407–409. doi:10.1016/S0041-624X(97)00021-8
- Torres, M. E., McManus, J., Hammond, D. E., de Angelis, M. A., Heeschen, K. U., Colbert, S. L., et al. (2002). Fluid and Chemical Fluxes in and Out of Sediments Hosting Methane Hydrate Deposits on Hydrate Ridge, OR, I: Hydrological Provinces. *Earth Planet. Sci. Lett.* 201, 525–540. doi:10.1016/S0012-821X(02)00733-1
- Tsai, C.-H., Hsu, S.-K., Chen, Y.-F., Lin, H.-S., Wang, S.-Y., Chen, S.-C., et al. (2019). Gas Plumes and Near-Seafloor Bottom Current Speeds of the Southernmost Okinawa Trough Determined from Echo Sounders. *Terr. Atmos. Ocean. Sci.* 30, 649–674. doi:10.3319/TAO.2019.07.07.01
- Turco, F., Ldroit, Y., Watson, S. J., Seabrook, S., Law, C. S., Crutchley, G. J., et al. (2022). Estimates of Methane Release from Gas Seeps at the Southern Hikurangi Margin, New Zealand. *Front. Earth Sci.* 10, 834047. doi:10.3389/feart.2022.834047
- Urban, P., Köser, K., and Greinert, J. (2017). Processing of Multibeam Water Column Image Data for Automated Bubble/seep Detection and Repeated Mapping. *Limnol. Oceanogr. Methods* 15, 1–21. doi:10.1002/lom3.10138
- Urban, P., Veloso-Alarcón, M., and Greinert, J. 2022 Echo Grid-Integration: A Novel Approach for Preprocessing Multibeam Water Column Data to Quantify Underwater Gas Bubble Emissions. Submitted to *L&O Methods*.
- Veloso, M., Greinert, J., Mienert, J., and De Batist, M. (2015). A New Methodology for Quantifying Bubble Flow Rates in Deep Water Using Splitbeam Echosounders: Examples from the Arctic Offshore NW-S Valbard. *Limnol. Oceanogr. Methods* 13, 267–287. doi:10.1002/lom3.10024
- Veloso-Alarcón, M. E., Jansson, P., De Batist, M., Minshull, T. A., Westbrook, G. K., Pälke, H., et al. (2019). Variability of Acoustically Evidenced Methane Bubble Emissions Offshore Western Svalbard. *Geophys. Res. Lett.* 46, 9072–9081. doi:10.1029/2019GL082750
- Wallmann, K., Riedel, M., Hong, W. L., Patton, H., Hubbard, A., Pape, T., et al. (2018). Gas Hydrate Dissociation off Svalbard Induced by Isostatic Rebound rather Than Global Warming. *Nat. Commun.* 9, 83. doi:10.1038/s41467-017-02550-9
- Wang, B., Jun, I., Socolofsky, S. A., DiMarco, S. F., and Kessler, J. D. (2020). Dynamics of Gas Bubbles from a Submarine Hydrocarbon Seep within the Hydrate Stability Zone. *Geophys. Res. Lett.* 47, 9. e2020GL089256. doi:10.1029/2020GL089256
- Wang, B., Socolofsky, S. A., Breier, J. A., and Seewald, J. S. (2016). Observations of Bubbles in Natural Seep Flares at MC 118 and GC 600 Using *In Situ* Quantitative Imaging. *J. Geophys. Res. Oceans* 121, 2203–2230. doi:10.1002/2015JC011452
- Wang, B., and Socolofsky, S. A. (2015). On the Bubble Rise Velocity of a Continually Released Bubble Chain in Still Water and with Crossflow. *Phys. Fluids* 27, 103301. doi:10.1063/1.4932176
- Weber, T. C., Mayer, L., Jerram, K., Beaudoin, J., Rzhanov, Y., and Lovalvo, D. (2014). Acoustic Estimates of Methane Gas Flux from the Seabed in a 6000 Km² region in the Northern Gulf of Mexico. *Geochem. Geophys. Geosyst.* 15, 1911–1925. doi:10.1002/2014GC005271
- Weber, T., Wiseman, N. A., and Kock, A. (2019). Global Ocean Methane Emissions Dominated by Shallow Coastal Waters. *Nat. Commun.* 10, 4584. doi:10.1038/s41467-019-12541-7
- Westbrook, G. K., Chand, S., Rossi, G., Long, C., Bünz, S., Camerlenghi, A., et al. (2008). Estimation of Gas Hydrate Concentration from Multi-Component Seismic Data at Sites on the Continental Margins of NW Svalbard and the Storegga Region of Norway. *Mar. Petroleum Geol.* 25, 744–758. doi:10.1016/j.marpetgeo.2008.02.003
- Westbrook, G. K., Thatcher, K. E., Rohling, E. J., Piotrowski, A. M., Pälke, H., Osborne, A. H., et al. (2009). Escape of Methane Gas from the Seabed along the West Spitsbergen Continental Margin. *Geophys. Res. Lett.* 36, 5. doi:10.1029/2009GL039191

Conflict of Interest: The authors declare that the research was conducted in the absence of any commercial or financial relationships that could be construed as a potential conflict of interest.

Publisher's Note: All claims expressed in this article are solely those of the authors and do not necessarily represent those of their affiliated organizations, or those of the publisher, the editors, and the reviewers. Any product that may be evaluated in this article, or claim that may be made by its manufacturer, is not guaranteed or endorsed by the publisher.

Copyright © 2022 Veloso-Alarcón, Urban, Weiss, Köser, She and Greinert. This is an open-access article distributed under the terms of the Creative Commons Attribution License (CC BY). The use, distribution or reproduction in other forums is permitted, provided the original author(s) and the copyright owner(s) are credited and that the original publication in this journal is cited, in accordance with accepted academic practice. No use, distribution or reproduction is permitted which does not comply with these terms.